Ore Geology Reviews 198 (2026) 107578

Contents lists available at ScienceDirect

Ore Geology Reviews

journal homepage: www.elsevier.com/locate/oregeorev

Lithostructural mapping and gold mineralization targeting in the Soaorib area, South Eastern Desert, Egypt: Insights from multi-sensor remote sensing, field studies and structural analysis

Ahmed I. Salem [a], Ali Shebl [b,c,*], Abdel-Kader M. Moghazi [a], Mohamed Abd El Monsef [b], Mahmoud K. Alawy [a]

[a] Geology Department, Faculty of Science, Alexandria University, 21511, Egypt
[b] Geology Department, Faculty of Science, Tanta University, 31527, Egypt
[c] Department of Mineralogy and Geology, Faculty of Science and Technology, University of Debrecen, Egyetem tér 1, Debrecen 4032, Hungary

ARTICLE INFO

Keywords:
Arabian-Nubian shield
Eastern desert of Egypt
Remote sensing
GIS
Geological mapping
Shear zones
Orogenic gold

ABSTRACT

The effective identification of mineralization targets during mineral exploration strategies depends on detailed lithological mapping and precise assessment of the structural patterns. The Soaorib area, in the South Eastern Desert (SED) of Egypt, comprises a late Neoproterozoic basement complex hosting a vein-type gold mineralization with limited information about its extent and distribution. This study integrates multi-sensor remote sensing data with field, structural, and petrographic investigations to map rock units, understand factors controlling gold mineralization, and delineate prospective mineralized zones for future exploration. Lithological discrimination revealed several rock units including gneisses, ophiolitic rocks, arc metavolcano-sedimentary association, metagabbro-diorite complex and granitic rocks of tonalitic to granodioritic composition. Hydrothermal alteration mapping, supported by field and petrographic verification revealed extensive alteration types such as phyllic, propylitic, ferrugination and carbonatization. Structural analysis reveals multiple deformation phases (D1–D3) documenting tectonic evolution from early arc-accretionary compression, through continental collision, to subsequent transpressional deformation, followed by minor late brittle overprinting. Gold mineralization is spatially confined to the NNE- and NNW-trending structures related to the late transpressional D3 phase. A Gold potentiality map (GPM) was generated using weighted overlay analysis (WOA) by integrating the principal lithostructural controls on gold mineralization in the study area. The resulting map highlights the most prospective zones and provides a practical framework for supporting mineral exploration in similar terranes.

1. Introduction

The Arabian Nubian Shield (ANS) covers ~610,000 km^2 on both sides of the Red Sea (Fig. 1a), extending westward into the Nubian Shield and eastward into the Arabian Shield (Kusky et al., 2003; Stern, 1994; Johnson et al., 2011). The ANS represents an orogenic belt developed between East and West Gondwana blocks that collided together forming Greater Gondwana during the late Neoproterozoic era (e.g. Stern, 1994; Johnson and Woldehaimanot, 2003; Collins and Pisarevsky, 2005; Gray et al., 2008). The crust of the ANS constitutes the largest Neoproterozoic juvenile one on Earth (Patchett and Chase, 2002). It was formed through a series of orogenic cycles linked to the breakup of the Rodinia supercontinent, the birth of the Mozambique Ocean (~850–780 Ma; Li et al., 2008), the generation of oceanic island arcs (~850–650 Ma), the amalgamation of the island arc terranes along ophiolite-decorated suture zones, and finally the collision between East and West Gondwana (650–550 Ma, Fritz et al., 2013). This tectonic history of the ANS was divided into three stages, namely: late Tonian-Cryogenian arc accretion stage (850–650 Ma), collision stage, and Ediacaran post-collision stage (635–550 Ma) (Stern, 1994; Kusky et al., 2003, Johnson and Woldehaimanot, 2003; Johnson et al., 2011). Metallogenetically, the ANS was adopted as one of the most significant Neoproterozoic gold resources on Earth (Zoheir et al., 2019; Johnson et al., 2017) with hundreds of documented gold occurrences (Johnson

* Corresponding author at: Department of Mineralogy and Geology, Faculty of Science and Technology, University of Debrecen, Egyetem tér 1, 4032 Debrecen, Hungary.
E-mail addresses: ali.shebl@science.tanta.edu.eg, rady.ali.shebl.ali.elshazly@science.unideb.hu (A. Shebl).

https://doi.org/10.1016/j.oregeorev.2026.107578
Received 27 March 2026; Received in revised form 28 September 2026; Accepted 28 September 2026
Available online 30 September 2026
0169-1368/© 2026 The Authors. Published by Elsevier B.V. This is an open access article under the CC BY-NC license (http://creativecommons.org/licenses/by-nc/4.0/).

et al., 2017; Botros, 2002; Almond et al., 1984; Tadesse et al., 2003; Ghebreab et al., 2009). The majority of these gold occurrences are structurally controlled and are related to major orogenic events in the development of the ANS, including the accretionary and the post-accretionary events (Harraz and Ashmawy, 1994; Sabet and Bordonosov, 1984; Abu-Alam et al., 2018; Helmy et al., 2004; Zoheir, 2012a; Zoheir et al., 2019; El Hebiry, 2021; Badawi et al., 2023; Abd El Monsef, 2025; Mesbah et al., 2026).

The Eastern Desert (ED) of Egypt represents the northwestern part of the ANS and has a long history of gold extraction, with more than 100 recorded mining sites within the Precambrian basement rocks (Fig. 1b), suggesting extensive mining activity over several millennia (Klemm and Klemm, 2013). Three principal styles of gold deposits are recognized in the ED, which are: orogenic, intrusion-related, and gold-bearing volcanogenic massive sulphides (VMS), in addition to placer deposits (Johnson et al., 2017; Zoheir et al., 2019; El Aref et al., 2020; Abd El Monsef, 2025). Nevertheless, the majority of these deposits correspond to vein-type orogenic gold systems and occur in a wide range of host rocks, including schists, metavolcanics, serpentinites, metagabbros, and granitoids (Harraz and El-Dahhar 1993; Hilmy and Osman 1989; Helmy et al., 2004; Abd El-Wahed et al., 2016, Zoheir, 2008; Abd El Monsef et al., 2018; Abd El Monsef and Abdelnasser, 2021; Zoheir et al., 2022; Khedr et al., 2024; Mesbah et al., 2026). The ED has considerable potential for undiscovered gold deposits, which may occur along major structures (structurally controlled) in ophiolitic and island-arc terranes or as dispersed sulfide mineralization within shear zones (Zoheir, 2011).

Remote sensing has become a powerful and widely adopted tool in mineral exploration, providing an efficient framework for regional-scale lithological discrimination and the detection of hydrothermal alteration zones. Spectral mapping leverages the spectral signatures of rock forming minerals captured by satellite sensors, enabling the identification of lithological units and alteration mineral assemblages associated with mineralized systems (Traore et al., 2020; van der Meer et al., 2012; Fossi et al., 2021; Pour et al., 2018, 2021). These approaches are particularly effective in arid terrains, where field accessibility is limited, and have been successfully applied in the South Eastern Desert of Egypt to support mineral exploration projects (Abd El-Wahed et al., 2023; Zoheir and Emam, 2014; Shebl et al., 2021, 2022, 2023). However, translating these datasets into a reliable understanding of the lithostructural controls of gold mineralization remains a major challenge, particularly in the structurally complex terranes of the ANS. A comprehensive suite of advanced image-processing techniques was applied for the first time in the Soaorib area by integrating multispectral satellite data (Landsat 9, Sentinel 2A, and ASTER) with PRISMA hyperspectral data, together with field and petrographic investigations to verify and refine the remote sensing interpretation. This integrated workflow significantly improved the existing geological map by refining lithological contacts, distinguishing previously undifferentiated rock units, and providing a more reliable interpretation on the lithostructural controls of gold mineralization. These improvements enabled the generation of a GIS-based gold potentiality map that delineates prospective mineralization zones in the study area.

2. General geological setting

The Precambrian basement rocks in the ED of Egypt represent part of the late Neoproterozoic ANS orogenic belt. Two significant mega-shear zones (the dextral NE-SW Qena-Safaga mega-shear and the sinistral NW-

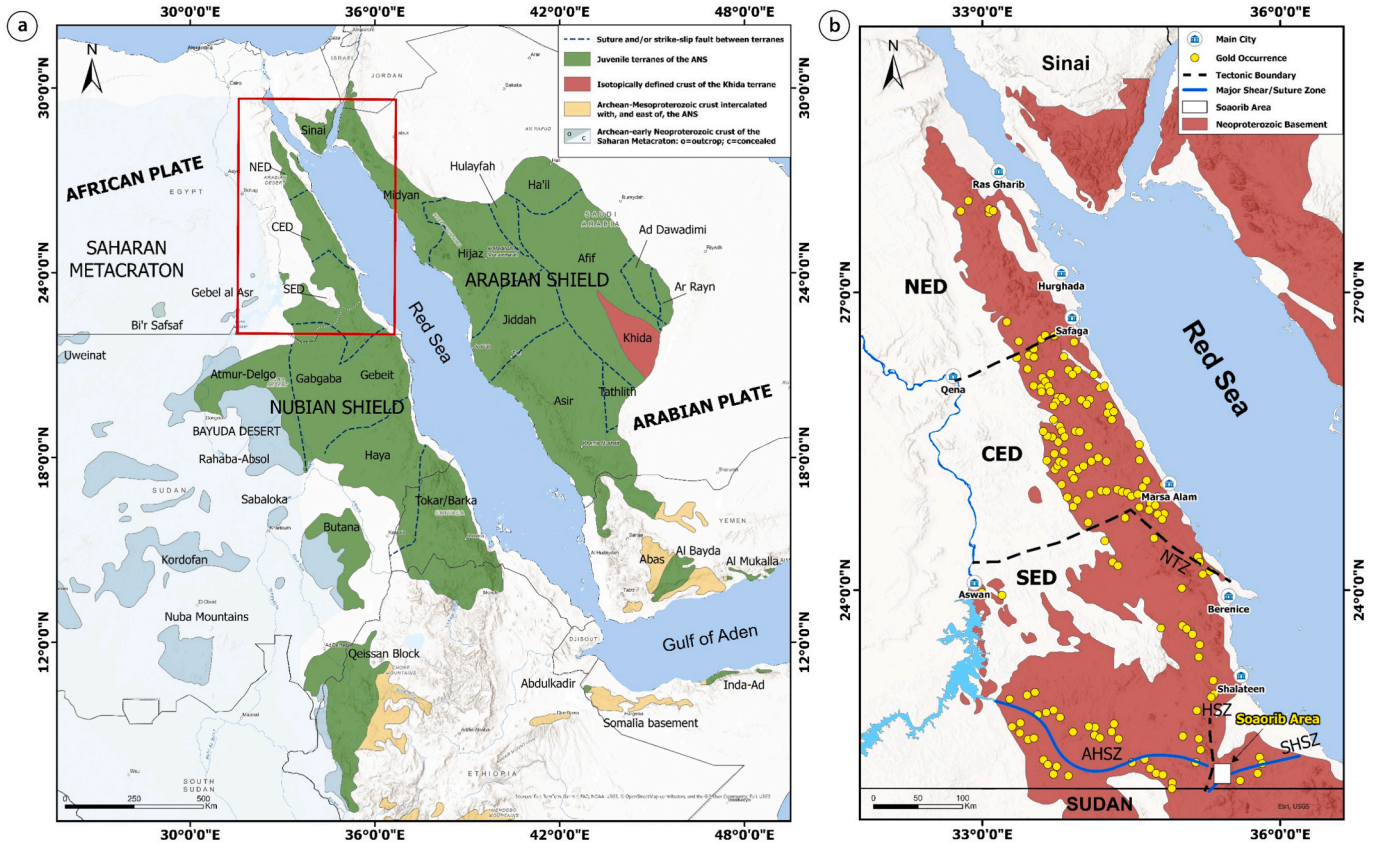


Fig. 1. (a) Regional geologic map of the ANS (modified after Johnson et al., 2011) showing the accreted arc terranes, ophiolite-decorated sutures, and Precambrian rocks of different ages. (b) Map of the Eastern Desert of Egypt showing the spatial distribution of the known gold occurrences and the location of the Soaorib area (modified after El Ramly, 1972; Botros, 2002; Zoheir et al., 2019; El Hebiry 2021). Abbreviations: NED=North Eastern Desert, CED=Central Eastern Desert, SED=South Eastern Desert (SED), NTZ=Nugrus thrust zone that separates the CED and SED, AHSZ and SHSZ are the Allaqi-Heiani and Sol Hamed accretionary suture zones, respectively that marks the southern boundary of the SED, HSZ=Hamisana post accretionary shear zone.

SE Nugrus thrust zone) (Fig. 1b) intersect these rocks and divide the ED into three unique terranes with different geological characteristics. These terranes are North Eastern Desert (NED), Central Eastern Desert (CED), and South Eastern Desert (SED) (Stern and Hedge, 1985). The NED is dominated by post-collision Ediacaran igneous and sedimentary rocks such as Dokhan volcanics, Hammamat molasse sediments, and younger granites (Stern and Ali, 2020). The CED was separated from the NED by the Qena-Safaga mega-shear and encompasses Tonian-Cryogenian ophiolitic rocks, arc metavolcano-sedimentary associations, gneisses, and *syn*-tectonic granitoids. The CED also includes Ediacaran igneous and sedimentary rocks along with deformation features like the post-accretionary NW-SE trending Najd-Fault System (NFS) (Stern, 1985; Alawy et al., 2025b). The boundary between the CED and the SED is represented by a mylonitic mega-shear zone known as Nugrus thrust zone (NTZ, Fig. 1b). The southern boundary of the SED is defined by the ~750–720 Ma Allaqi-Heiani (AHSZ) and Sol Hamed (SHSZ) accretionary suture zones (Fig. 1b) that marked by suprasubduction ophiolitic belts (Abdelsalam and Stern, 1996; Abdeen and Abdelghaffar, 2011; Stern et al., 1990). The Allaqi-Heiani-Sol Hamed suture zone was cut by a post-accretionary trending N-S shear zone (~50 km wide and 300 km long), known as the Hamisana shear zone (HSZ; Fig. 1b), which extends from northern Sudan into the Egyptian SED (Miller and Dixon, 1992; Stern et al., 1989; de Wall et al., 2001). Stern et al. (1989) suggest that the HSZ and the NFS are genetically contemporaneous, linking both structures to the Najd tectonic cycle (~640 Ma). Lithologically, the SED is dominated by gneisses, migmatites, and gneissose granites with ages between ~675 to 700 Ma (Kröner et al., 1994). Complete ophiolite sequences together with ophiolitic mélange occurrences represent suprasubduction forearc ophiolites in the SED (Ahmed, 2013; Zimmer et al., 1995; Abdel-Karim et al., 2016, 2021; Azer et al., 2013; Gahlan et al., 2015; Khedr and Arai, 2013) and have been dated between 741 and 713 Ma (Kröner et al., 1992; Ali et al., 2010; Zoheir et al., 2022; Diab et al., 2026). There are also several exposures of arc-related metavolcano-sedimentary rocks, with an estimated age of ~711 ± 24 Ma (Stern et al., 1990). Additionally, several mafic–ultramafic Alaskan-type intrusion complexes are recorded in the central part of the SED (Helmy and El Mahallawi 2003; Helmy et al., 2014; Khedr and Arai 2016; Azer et al., 2017). Despite hosting many gold deposits exploited since Pharaonic times, the SED remains underexplored due to its remoteness and limited infrastructure. Over the last decade, fascination with scientific research and exploration of SED has begun to grow; nevertheless, many areas still require further investigation.

The Soaorib area, the focus of this study, is located between latitudes 22° 15′ and 22° 03́N and longitudes 35° 30′ and 35° 20́E, covering ~380 km^2 of the Precambrian basement complex of the SED (Fig. 1b). Previous studies on this area mapped the rock units differently. Khudeir et al.

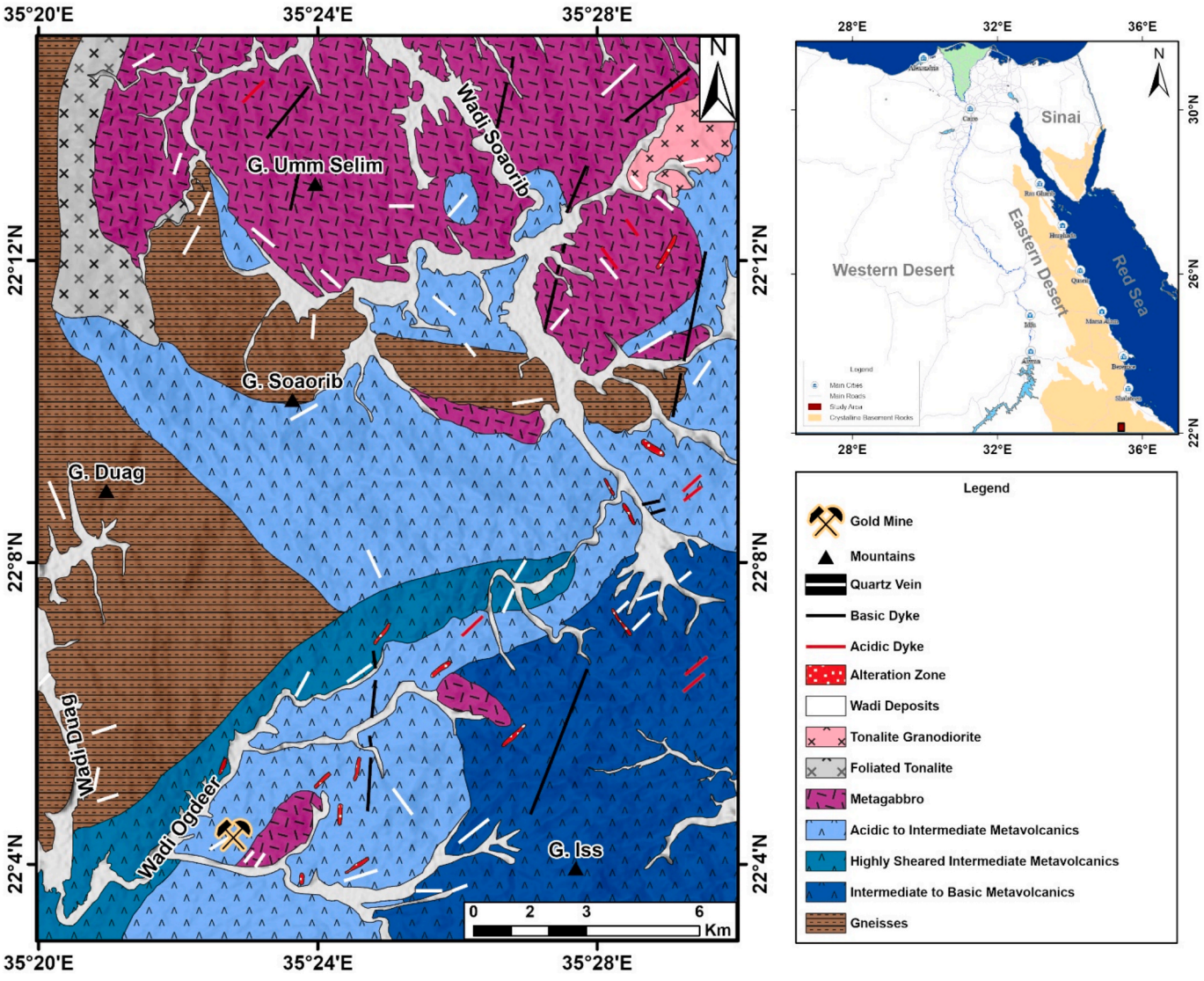


Fig. 2. General geologic map of the Soaorib area (modified after SMRC, 2018).

(2003) mapped the G. Soaorib as medium to high grade gneisses and migmatites with some Dokhan volcanics in the southern part. They also marked G. Umm Selim as hornblende gabbro, G. Duag (El Kazzaz, 2012) as syn- to late-orogenic granitoids and G. Iss as metavolcanics. Makhlouf (2008) constructed a regional scale geological map of the Soaorib area including gneisses, ophiolitic fragments, metasediments, metavolcanics and gabbro. Ali-Bik et al. (2014) mapped the Soaorib area as gneisses, metavolcanics with pillow lava, acidic to intermediate metavolcanics, gabbro-diorite, and older granitoids. SMRC (2018, 2021, 2023) discriminated the basement rock units of the area to gneisses, intermediate to basic metavolcanics, extensively sheared intermediate metavolcanics, acidic to intermediate metavolcanics, metagabbro, and granitoids of tonalitic and granodioritic composition (Fig. 2). These units are intersected by mafic and felsic dykes, in addition to quartz veins surrounded by various alteration zones (SMRC, 2018). Structurally, Khudeir et al. (2003) identified three deformational phases (D1-D3), where D1 is related to orogenic stresses that caused thrusting of the ophiolitic nappes, D2 is obviously related to the stresses associated with the development of the HSZ, and D3 is also genetically related to the dextral shearing movement along the HSZ. Makhlouf (2008), on the other hand, identified five deformation phases in the same area. Based on the different approaches applied in this work, several modifications have been introduced to the lithostratigraphic units as well as to the geologic map, and these are presented and discussed in the following sections.

3. Materials and methods

3.1. Materials

The satellite datasets utilized in this study are derived from both multi-spectral and hyperspectral sensors, each sensor was employed toward a specific objective. Multispectral sensors include Landsat 9, Sentinel 2A, and ASTER, while hyperspectral sensors are represented by the PRISMA satellite. Landsat 9 was utilized for lithological and structural mapping because of its enhanced radiometric resolution (14-bit) (Xu et al., 2024; Niroumand-Jadidi et al., 2022; Shebl et al., 2024), whereas Sentinel 2A was used in lineament investigations owing to its 10 m spatial resolution (Alaoui et al., 2025; Karim et al., 2021). With outstanding spectral ranges of VNIR and SWIR bands, ASTER offers the ability to distinguish between various hydrothermal alteration minerals (Abdel-Rahman et al., 2023; Chen et al., 2022). The PRISMA hyperspectral sensor was employed to perform accurate spectral profiling, providing detailed insights into the mineralogical composition of the

Table 1
Characteristics of the utilized satellite sensors.

Satellite	Bands	Wavelength (nm)	Spectral Region	Spatial Resolution (m)	No. of Bands	Objective
Landsat 9	B1	430–450	Coastal aerosol	30	11	Lithological & Structural Mapping
	B2	450–510	Blue			
	B3	530–590	Green			
	B4	640–670	Red			
	B5	850–880	NIR			
	B6	1570–1650	SWIR 1			
	B7	2110–2290	SWIR 2			
	B8	500–680	Panchromatic	15		
	B9	1360–1380	Cirrus	30		
	B10	10600–11190	TIRS 1	100		
	B11	11500–12510	TIRS 2			
ASTER	B1	520–600	VNIR	15	14	Hydrothermal Alteration Zones Mapping
	B2	630–690				
	B3N	780–860				
	B3B	780–860				
	B4	1600–1700	SWIR	30		
	B5	2145–2185				
	B6	2185–2225				
	B7	2235–2285				
	B8	2295–2365				
	B9	2360–2430				
	B10	8125–8475	TIR	90		
	B11	8475–8825				
	B12	8925–9275				
	B13	10250–10950				
	B14	10950–11650				
Sentinel 2	B1	443	Ultra-Blue	60	12	Automatic Lineament Extraction
	B2	490	Blue	10		
	B3	560	Green			
	B4	665	Red			
	B5	705	Red Edge1	20		
	B6	740	Red Edge2			
	B7	783	Red Edge3			
	B8	842	NIR	10		
	B8A	865	VNIR (narrow)	20		
	B9	940	Water Vapor	60		
	B10	1375	SWIR (Cirrus)			
	B11	1610	SWIR1	20		
	B12	2190	SWIR2			
PRISMA	66 Bands	400–1010	VNIR	30	242	Hyperspectral
	174 Bands	920–2505	SWIR			Data Analysis
	PAN	–	–	5		

mapped rock units (Habashi et al., 2024; Alawy et al., 2025a). The characteristics of each sensor, along with its corresponding objective, are summarized in Table 1. All processing and preprocessing activities were carried out using a collection of geospatial software including ENVI 5.6, ArcGIS Pro 3.6, Rockworks 16 and PCI Geomatica 2016.

A cloud-free Landsat 9 scene (LC09_L1TP_172045_20240525_20240525_02_T1, May 2024, USGS) was preprocessed with radiometric and atmospheric corrections, spatial subsetting, and Gram–Schmidt pan-sharpening to achieve a resolution of 15 m. A Sentinel-2 Level-1C scene (S2A_MSIL1C_20241207T081331_N0511_R078_T36QYK_20241207 T090119, December 2024, ESA) was corrected using FLAASH, stacked, resampled to 10 m, and limited to the study area. An ASTER scene (AST_L1T_00302202007081912_20150518084833_86937, 2007, USGS) was preprocessed with radiometric and atmospheric corrections, VNIR–SWIR stacking, resampling to 15 m, and subsetting, selected because the SWIR subsystem failed after 2008. Two PRISMA hyperspectral scenes (PRS_L2D_STD_20220201082205_20220201082210_0001, 2022, ISA) and (PRS_L2D_STD_20220201082201_20220201082205_0001, 2022, ISA) comprising 250 bands (0.4–2.5 μm), were preprocessed by stacking, noisy band removal, and spatial subsetting. Furthermore, geological maps and previous studies (e.g. El Baghdady et al., 2002; El Shimi et al., 2012; SMRC, 2018, 2021, 2023) were compiled to support satellite image interpretation and the development and validation of GPM. All spatial datasets were georeferenced and projected to the UTM Zone 36 N coordinate reference system using the WGS 1984 datum to ensure spatial consistency throughout the study.

3.2. Methods

The methodology adopted in this study integrated satellite image processing, field and petrographic investigations, structural analysis and mapping, and GPM to investigate the lithostructural controls on gold mineralization in the Soaorib area. The overall methodological workflow is presented in Fig. 3.

3.2.1. Satellite image processing techniques

False Color Composites (FCC): It is an effective technique that enhances visual inspection of lithological contacts and major structures by combining selected spectral bands into composite images with false colors (Shebl et al., 2021; Abd El-Wahed et al., 2023). Stretching techniques were utilized to enhance the contrast and saturation of colors for enhanced visual inspection.

Band Ratios (BR) and Band Math (BM): These techniques involve dividing DN values of pixels through either straightforward division (i.e. one band divided by another) or through mathematical equations (i.e., band math). Single channel division results in a greyscale image, whereas importing a ratio in each RGB channel results in a colored composite. These ratios highlight the unique spectral response variations among rocks in specific wavelength ranges. The band ratio technique was widely applied in mineral exploration projects for precise lithological mapping (Abd El-Wahed et al., 2023; Ge et al., 2018; Abd El-Wahed et al., 2021).

Principal Component Analysis (PCA): It is a statistical approach employed to decrease dimensionality by transforming correlated spectral bands into a series of uncorrelated principal components (Dawoud et al., 2023; Abd El-Wahed et al., 2023). Most of information is captured in the first few PCAs, whereas the remaining PCAs contain noise. Therefore, the first three PCAs were utilized to create certain band combinations which were highly effective in highlighting specific rock units (Sultan et al., 1986; Zoheir et al., 2018; Abd El-Wahed et al., 2021).

Band Threshold Technique on Mineral Indices: This technique uses mineral indices obtained from ASTER data to delineate hydrothermal alteration zones and has demonstrated considerable effectiveness in mineral exploration (Rowan and Mars, 2003; Hewson et al., 2006; Ninomiya et al., 2005; Yajima and Yamaguchi, 2013; Hassan and Ramadan, 2015). Pixels exhibiting the highest reflectance values within pre-defined threshold ranges were extracted to identify the spatial distribution of alteration minerals. ASTER bands sensitive to alteration minerals were utilized, and threshold values were calculated using the formula: Band Threshold = Mean + (2 × Standard Deviation). Table 2 illustrates the applied equations.

Hyperspectral remote sensing, covering 0.4–2.5 μm, allows precise lithological mapping by recording diagnostic absorption features of rocks through hundreds of narrow spectral bands (Feng et al., 2018; Shebl et al., 2023). In this study, the PRISMA satellite is employed for the first time on the study area to analyze the spectral reflectance curves of the mapped lithological units and alteration zones with obvious anomalies. The spectral reflectance curves of the alteration zones were created by extracting representative spectra from homogeneous clusters of anomalous pixels found within each identified alteration type (phyllic, propylitic, ferruginous, and carbonatization). Efforts were made to choose spectrally pure pixels distant from boundaries to avoid mixing effects. This method yielded two complementary evaluations: (1) lithological profiling, based on representative spectral reflectance curves of each rock unit, enabling direct comparison among all mapped lithologies, and (2) alteration profiling to identify diagnostic absorption features for phyllic, propylitic, ferruginous, and carbonatization/listwaenite zones. The integration of these two approaches combines visual image interpretation with diagnostic spectral signatures, providing complementary information for lithological discrimination and hydrothermal alteration mapping.

3.2.2. Field work and petrography

A field campaign was conducted in the study area to verify the remote sensing interpretation, study lithological contacts, collect representative rock samples, and identify and measure geological structures. Field measurements were limited because they were primarily acquired to verify remotely sensed structures and establish field relationships between mineralized zones and the surrounding country rocks, depending on the accessibility within the study area. In addition, systematic GPS-referenced samples of quartz veins, alteration zones, and representative country rocks were collected. Petrographic investigation of the collected samples was conducted to verify the field and remote sensing interpretations and refine the characterization and nomenclature of the mapped rock units. Thirty thin sections prepared from alteration zones and country rocks were examined using a polarized light microscope. The study focused on identifying their mineralogical composition, textures, and mineral assemblages resulting from hydrothermal alteration. This analysis was carried out at the Mineral Resources Center, Department of Geology, Faculty of Science, Alexandria University, utilizing an Olympus polarized light microscope fitted with a digital camera.

3.2.3. Structural analysis and mapping

Automatic lineament extraction and trend analysis provide an effective approach for mineral exploration, particularly in areas where hydrothermal mineral deposits are structurally controlled by fracture zones (Bannari et al., 2016; Abd El-Wahed et al., 2021). Thus, mapping lineaments facilitates the identification of concealed mineralization and dilation zones and enhances predictive targeting of structurally controlled ore systems. In this study, lineaments were extracted from the first principal component (PC1) generated from Sentinel 2 imagery that was chosen for its ability to retain most of the spectral information along with a comparatively high spatial resolution (10 m). The algorithm of the LINE module implemented in PCI Geomatica software was utilized for automated lineaments extraction. Parameter values were optimized through a trial-and-error strategy to maximize the extraction of geologically meaningful lineaments, particularly those aligned with the major structural features observed through ground truth and on satellite imagery. The essential parameters were configured as follows: filter radius = 10, edge gradient threshold = 50, curve length threshold = 30, line fitting threshold = 3, angular difference threshold = 30, and linking

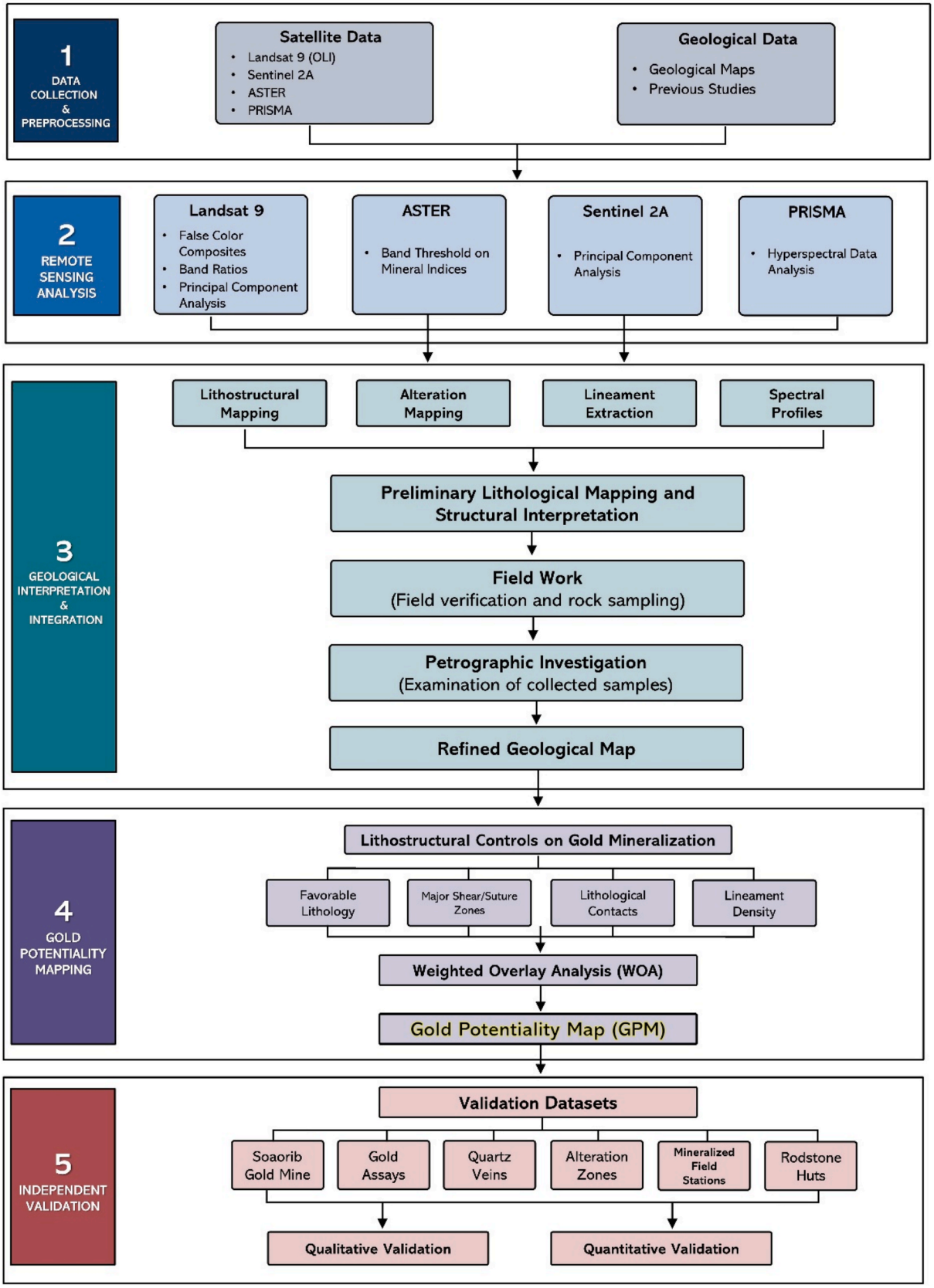


Fig. 3. Methodological workflow adopted in the current study, showing the sequential steps of data collection, remote sensing analysis, geological interpretation and integration, gold potentiality mapping and subsequent validation.

Table 2
ASTER mineral indices applied for detecting hydrothermal alteration minerals in the study area.

SR	Index name	Mineral assemblage	Equation	Reference
1	Ferric Iron (Fe^{3+}) Alteration Index	hematite, goethite and jarosite	b2/b1	Rowan and Mars, 2003; Hewson et al., 2006; Mamouch et al., 2022
2	Ferrous Iron (Fe^{2+}) Alteration Index	actinolite, chlorite, ankerite and siderite	(b5/b3) + (b1/b2)	Rowan and Mars, 2003
3	Propylitic Alteration Index	carbonates, chlorite and epidote	(b7 + b9)/b8	Rowan and Mars, 2003; Mamouch et al., 2022
4	Phyllic Alteration Index	sericite, muscovite, illite and smectite	(b5 + b7)/b6	Rowan and Mars, 2003; Hewson et al., 2006; Mamouch et al., 2022
5	Hydroxyl (OH) Group Index	serpentinite, talc Al–O–H, Mg–O–H, Si–O–H, and CO3Ferromagnesian Minerals	(b7/b6) × (b4/b6)	Ninomiya et al., 2005

distance threshold = 20. Extracted lineaments are subsequently exported as Esri shapefiles and imported into a developed ArcGIS Pro Model Builder workflow, where a fully automated spatial analysis and calculations along with density-based mapping are executed, and the final output was exported in CAD format. The last step involved importing the lineaments CAD file into Rockworks software, which creates a rose diagram showing the primary structural orientation of extracted lineaments.

Structural Mapping relies on careful visual inspection, spectral characteristics of Landsat 9 bands, and the structural architecture of the study area. Accordingly, we chose color composites that enabled a successful identification of the major geological structures. In addition, various structural elements were collected from the study area and plotted on equal-area, lower-hemisphere projections utilizing Stereonet software (version 11) developed by Richard W. Allmendinger.

3.2.4. Gold potentiality mapping (GPM)

GPM is effective in delineating prospective mineralized zones (Abd El-Wahed et al., 2023; Shebl et al., 2021, 2022; El-Desoky et al., 2022, 2023; Sun et al., 2019). The weighted overlay analysis (WOA) employed in this study is a knowledge-driven multicriteria decision analysis (MCDA) approach that integrates multiple factors using predefined weights to generate a GPM (Bonham-Carter, 1994; Carranza, 2008; Harris et al., 2015). Four spatial layers representing the principal lithostructural controls on gold mineralization in the Soaorib area were used: favorable lithologies, proximity to major shear zones, proximity to lithological contacts, and lineament density. To avoid circular reasoning, layers related to direct evidence of gold mineralization, including the Soaorib gold mine, positive gold assay locations, quartz veins, mineralized field stations, hydrothermal alteration zones, and rodstone huts, were excluded from the model inputs and used exclusively for independent validation. Prior to analysis, all layers were spatially standardized by projecting them into the WGS 84 /UTM Zone 36 N coordinate system and converting them into raster format with a uniform cell size of 15 m. Input layers were subsequently reclassified into a favorability scale ranging from 1 (very low) to 5 (very high) according to their relative importance to gold mineralization. Weights were derived using the Analytical Hierarchy Process (AHP), a multicriteria decision-making method in which pairwise comparisons are transformed into quantitative weights (Saaty, 1980). The assigned weights, data sources, and their corresponding geological rationale are summarized in Table 3. The consistency of the pairwise comparison matrix was evaluated using the Consistency Ratio (CR). The obtained CR value (0.0263) was below the acceptable threshold of 0.10, indicating that the assigned weights were sufficiently consistent, following the approach of Saaty (1980). Finally, the reclassified layers were integrated using the Weighted Overlay Analysis (WOA) tool in ArcGIS Pro 3.6 to generate the final GPM. The analysis was restricted to the lithological units, while wadi areas, occupying 48.215 km^2, were excluded from the analysis and treated as NoData. Consequently, the effective modeled area was 331.785 km^2.

The generated GPM was subsequently validated qualitatively through visual inspection by overlaying the mineralization-related evidence layers on the final GPM. Quantitative validation was performed by calculating the area and percentage of each potentiality class, number of validation points within each class, and the cumulative area and cumulative validation percentages. Finally, the performance of the model was assessed using the Success-rate curve, which compares the cumulative area with the cumulative validation percentages, together with the Enrichment Ratio (ER), which evaluates the concentration of validation points relative to a random spatial distribution (Chung and Fabbri, 2003; Carranza, 2009; Carranza and Laborte, 2015; Harris et al., 2025).

4. Results

4.1. Lithological mapping

Representative Landsat 9 image products were selected to illustrate the lithological discrimination achieved by each image processing technique (Table 4). The lithological interpretation derived from remote sensing data was verified by integrating field observations collected during the present study with lithological observations compiled from previous studies (e.g. El Baghdady et al., 2002; El Shimi et al., 2012; SMRC, 2018, 2021, 2023).

False Color Composites (FCC): The decorrelation-stretched FCC 753 effectively discriminated between the ophiolitic metavolcanics (Omv) and the arc metavolcanics (Mvs) in the southern part along the Ogdeer thrust (El Kazzaz, 2012) and near G. Iss (Fig. 4). The strong response in SWIR-2 (Band 7), displayed in the red channel, caused the Omv to appear in red, whereas assigning NIR (Band 5) to the green channel highlighted the Mvs in green tones. The enhanced contrast reflects the distinct spectral responses of the basaltic Omv and the more evolved andesitic–dacitic Mvs across the selected spectral bands, resulting in improved discrimination between the two metavolcanic rock units (Lillesand et al., 2015; USGS, 2022).

Band Ratios (BR) and Band Math (BM): The band-ratio composite (5/7, 4/5, and 3/1) proposed by Zoheir et al. (2018) enabled effective mapping of the ophiolitic metagabbro (Omgb) and the ophiolitic metavolcanics (Omv) around the Soaorib gold mine in the southern part of the study area (Fig. 5). The assigned red (5/7), green (4/5), and blue (3/1) channels display the ophiolitic metagabbro in pinkish–magenta tones, whereas the surrounding ophiolitic metavolcanics appear in bluish tones. It also outlined the metagabbro–diorite complex of G. Umm Selim in the northern part of the study area as a broad, rounded exposure distinct from its surroundings. The band-ratio composite (6/7, 6/2, and 6/5 × 4/5) proposed by Sultan et al. (1986) delineated the gneissic basement from the surrounding metagabbro-diorite rocks in the northern part of the study area, while also highlighting the gneissic basement and listwaenite bodies in the southern part (Fig. 6). The 6/7 ratio is sensitive to hydroxyl-bearing minerals, 6/2 emphasizes compositional variations associated with FeO-bearing rocks with mafic rocks generally exhibiting lower reflectance than felsic lithologies (Alarifi et al., 2022). Moreover, 6/5 × 4/5 enhances the distinction between mafic and non-mafic lithologies through its sensitivity to variations in Fe-bearing aluminosilicate minerals (Alarifi et al., 2022). Accordingly, gneisses appear green owing to their relatively stronger response in the 6/2

Table 3
Input layers and weighting scheme used in the Weighted Overlay Analysis (WOA).

SR	Thematic layer	Data type	Class ranges	Class rank (5–1)	Weight (%)	Data source	Geological rationale
1	Major Shear/ Suture Zones (Proximity)	Euclidean Distance	<0.5 km 0.5–1 km 1–1.5 km 1.5–2 km 2–3 km	5 4 3 2 1	42	Structural mapping	Regional structures provide first-order structural control on mineralization.
2	Lithological Contacts (Proximity)	Euclidean Distance	<0.5 km 0.5–1 km 1–1.5 km 1.5–2 km 2–3 km	5 4 3 2 1	27	Geological mapping supported by field observations	Contacts between contrasting lithologies act as zones of structural weakness and preferential fluid flow.
3	Lithological Units (Overlay)	Categorical (Discrete)	Omgb List Omv Mgb/Mvs Gd/Ton/Gn	5 4 3 2 1	12	Geological mapping supported by field observations and petrography	Host rocks exert strong lithological control on gold mineralization, particularly the altered ophiolitic metagabbro, listwaenites and metavolcanics.
4	Lineament Density (Overlay)	Continuous	Very High = 5, High = 4, Moderate = 3, Low = 2, Very Low = 1	5–1	19	Sentinel 2A Lineament extraction and density mapping	High fracture density enhances permeability and facilitates hydrothermal fluid migration.

Table 4
Representative Landsat 9 image products used for lithological mapping and the rationale for their selection.

SR	Image	Selection criteria	Geological objective	Reference
1	FCC 753 (decorrelation stretched)	Maximizing contrast between spectrally similar volcanic units in the visible, NIR and SWIR-2 wavelengths.	Separation of ophiolitic metavolcanics from arc metavolcanics.	USGS, 2022
2	Band ratio (5/7, 4/5, 3/1)	Enhancing spectral differences among lithologies by combining visible and IR wavelength ratios.	Mapping ophiolitic metagabbro and ophiolitic metavolcanics around the mine area.	Zoheir et al., 2018
3	Band ratio (6/7, 6/2, 6/5 × 4/5)	Improving discrimination between mafic and non-mafic rocks.	Delineation of gneisses and listwaenite bodies.	Sultan et al., 1986; Alarifi et al., 2022
4	PCA-312	Improving discrimination of lithologies with subtle spectral differences.	Separation of the metagabbro–diorite complex from foliated tonalite and granodiorite.	Lillesand et al., 2015; Sultan et al., 1986; Zoheir et al., 2018; Abd El-Wahed et al., 2021

channel, whereas the listwaenite bodies along Wadi Ogdeer are displayed as bright yellow because of their high responses in both the 6/7 and 6/2 channels reflecting the abundance of hydroxyl-bearing and carbonate minerals associated with listwaenitization. The metagabbro–diorite rocks are displayed in red tones, indicating a dominant relative contribution from the red channel (6/7) compared with the green and blue channels.

Principal Component Analysis (PCA): The PCA-312 composite clearly differentiated the metagabbro–diorite rocks from the foliated tonalite in the northwestern corner near G. Umm Selim, where a sharp intrusive contact is delineated. It also separated the granodiorite from the metagabbro–diorite rocks in the northeastern corner near Wadi Soaorib (Fig. 7).

Results from Landsat 9 image processing were used to enhance and modify the geological map of the Soaorib after SMRC (2018). The metaultramafic unit (listwaenite zones) along the Ogdeer thrust is mapped here for the first time. The metagabbro was subdivided into two distinct units: the ophiolitic metagabbro southward near the Soaorib Gold Mine, and the metagabbro–diorite complex northward around G. Umm Selim. Lithological contacts were further refined through visual interpretation of the satellite processing outputs. The mapped rock units are arranged in a well-defined lithostratigraphic sequence from oldest to youngest and the updated geological map is illustrated in Fig. 8.

4.2. Hydrothermal alteration mapping

Processing of ASTER datasets revealed several potential hydrothermal alteration zones in the Soaorib area (Fig. 9a–e), which show a strong spatial association with favorable lithological contacts and major fault systems. Four main types of alteration were mapped: (1) phyllic alteration, dominated by the sericitization of island arc metavolcanics, producing sericite and muscovite as well as minor quartz; (2) propylitic alteration, characterized by chloritization where secondary chlorite replaces mafic minerals in the ophiolitic metavolcanics, particularly metabasalts; (3) ferrugination, indicated by hematite, limonite, siderite and goethite formed in oxidized fractures and altered host rocks; and (4) carbonatization, defined by carbonate minerals (calcite ± dolomite) and secondary silica that form NE-SW-trending listwaenite sheets. These alteration signatures were verified petrographically and exhibit clear spatial connections with the main structural and lithological elements of the area. For example, the phyllic alteration is localized along the NE-SW Ogdeer thrust, which intersects the ophiolitic and island-arc metavolcanics (Fig. 9a). The propylitic alteration is primarily restricted to the ophiolitic metavolcanics located in the southeastern portion of the study area (Fig. 9b). Ferrugination is noted along the two major fault systems (Ogdeer and Duag thrusts) (Fig. 9c–d). Carbonatization or listwaenization preferentially occurs along lithological contacts between the metavolcanics and the gneissic country rocks, forming elongated NNE-SSW to NE-SW thrust sheets (Fig. 9e). Overall, the distribution of these alteration zones shows significant structural influence, where alteration is preferentially developed along major shear zones and lithological boundaries.

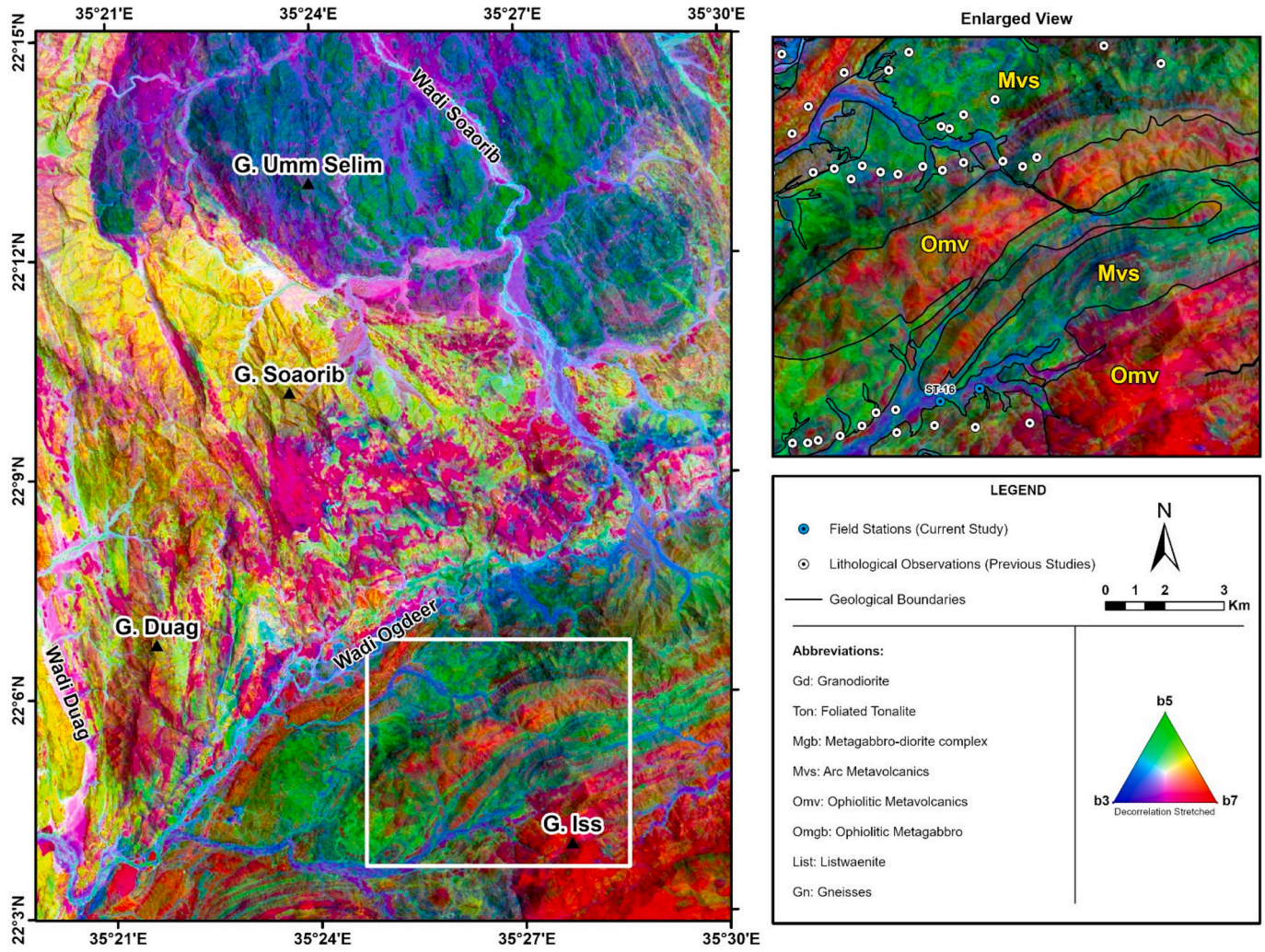


Fig. 4. Lithological discrimination using Landsat 9 false color composite (FCC 753; decorrelation stretched) in RGB. Representative field stations are labeled with their respective IDs to provide spatial cross-references to the field observations presented in subsequent figures. The prefix ST- denotes field stations.

4.3. Hyperspectral data analysis

The spectral reflectance curves of the mapped lithologies exhibit unique reflectance signatures (Fig. 10a-b). Typically, two distinct troughs appear near ~1400 nm and ~1900 nm; indicating atmospheric moisture or structural/adsorbed water within minerals (Hunt, 1977; Clark, 1999; Guanter et al., 2006). In agreement with earlier spectral studies (e.g. Hunt and Salisbury 1970, 1971; Madani et al., 2021; Jan et al., 2024; de Souza et al., 2024; Surour et al., 2025; Shebl et al., 2025), listwaenites display a relatively high reflectance and notable absorption characteristics, consistent with their carbonate-rich composition and make them the brightest unit in the study area. The granitoids (tonalite and granodiorite) exhibit moderately high and relatively smooth spectra with few weak absorptions, indicating their felsic intrusive nature and limited hydrothermal alteration. Gneisses show intermediate reflectance values and subdued absorption responses, consistent with their quartz–feldspar mineralogy. The metavolcano-sedimentary unit exhibits medium reflectance but more intense absorptions, reflecting alteration effects on its volcanic and sedimentary components. In contrast, the ophiolitic metavolcanics and metagabbros show the least reflectance and strongest absorptions, indicating their mafic composition and high susceptibility to hydrothermal alteration, which aligns with their function as mineralized host rocks in the Soaorib Gold Mine. The metagabbro–diorite complex lies in between and shows moderate reflectance and less intense absorptions than the ophiolitic units. Notably, the spectral responses of the two mapped gabbroic units (ophiolitic metagabbro and metagabbro–diorite complex) vary, which fully supports the lithological mapping (Fig. 10a). Overall, these spectral features provide a clear signature for every rock unit and enhance lithological mapping by adding spectral insights that confirm lithological variability obtained from our interpretation of multispectral data analysis.

Analysis of the spectral reflectance curves of the alteration zones reveals distinct differences among alteration types. Phyllic alteration is marked by moderate reflectance and a distinct absorption feature near ~2200 nm (Hunt, 1977; Pour and Hashim, 2012; Asadzadeh et al., 2024; Meyer et al., 2022; Abdellatif et al., 2025), indicating the dominance of phyllosilicate minerals like sericite and muscovite. Propylitic alteration shows lower overall reflectance with a pronounced absorption near ~2300 nm, reflecting the presence of chlorite and epidote in mafic host rocks (Meyer et al., 2022; Asadzadeh et al., 2024). Ferrugination is represented by two distinct spectra, which are Fe^{+2} and Fe^{+3}. The Fe^{+2} curve displays lower reflectance with wider absorption, particularly around ~900 nm (Asadzadeh et al., 2024) within the visible to near-infrared spectrum, indicating depletion of Fe^{+2} bearing minerals in altered rocks. The Fe^{+3} curve, on the other hand, demonstrates higher reflectance with sharper absorption near ~550 nm (Asadzadeh et al., 2024), indicative of oxidized surfaces rich in hematite and goethite. Carbonatization or listwaenization displays the highest reflectance of all alteration types, with diagnostic carbonate absorptions between ~2330 and 2500 nm, which verifies significant carbonation and silica

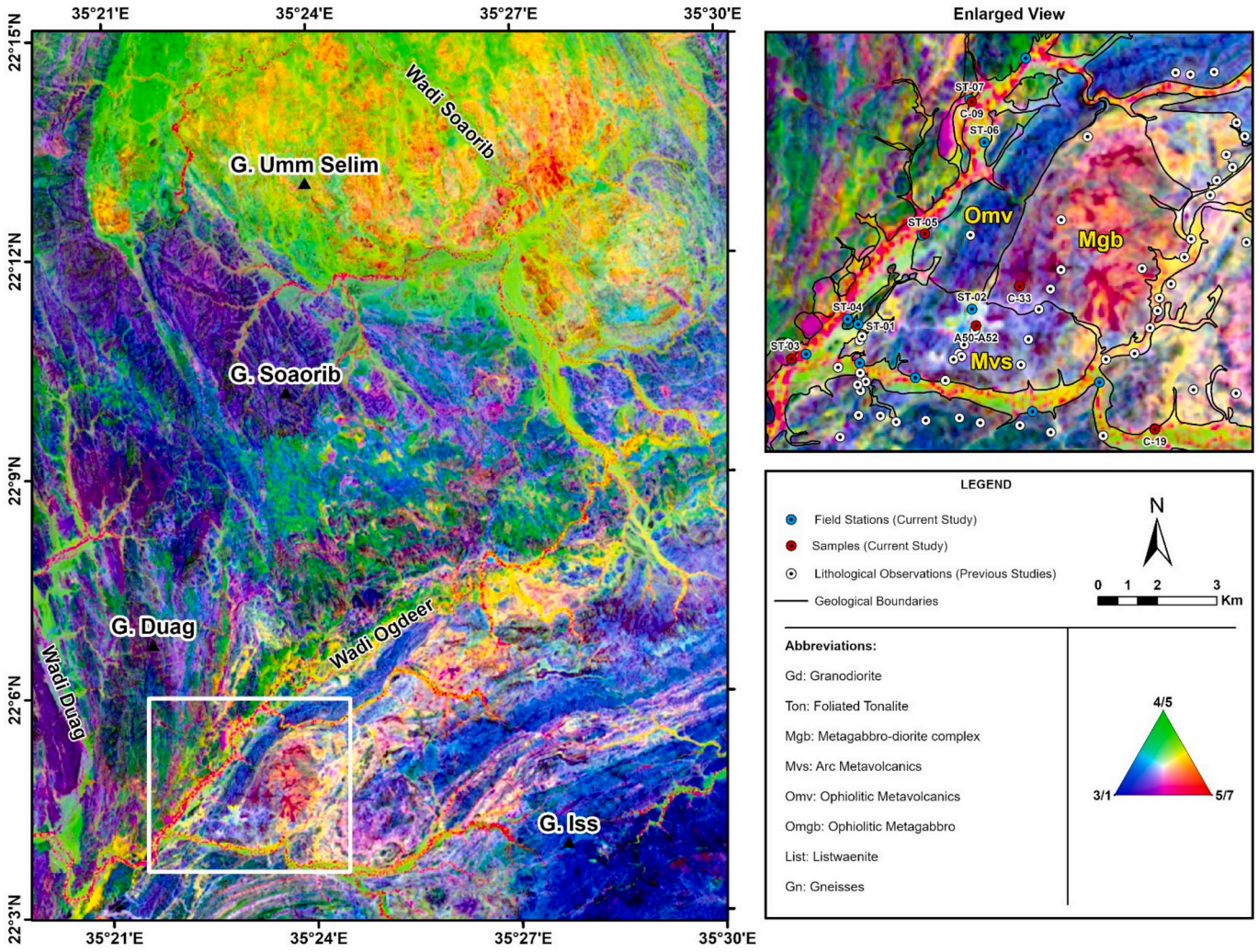


Fig. 5. Lithological discrimination using Landsat 9 band ratio composite (5/7, 4/5, 3/1) in RGB. Representative field stations and petrographic samples are labeled with their respective IDs to provide spatial cross-references to the field and petrographic observations presented in subsequent figures. The prefixes ST-, C-, and A- denote field stations, country-rock samples, and alteration-zone samples, respectively.

enrichment (Madani et al., 2021). Field observations reinforce these conclusions, as listwaenite zones are highly oxidized and often enriched with secondary goethite after pyrite cubes, which explains the similarity between the Fe^{3+} and carbonatization/listwaenization spectral curves (Fig. 10b).

4.4. Field work

Field investigations reveal the presence of five rock units in addition to numerous exposures of hydrothermally altered rocks. The main rocks units comprise gneisses, ophiolitic rocks, metavolcano-sedimentary associations, a metagabbro-diorite complex, and granitoid rocks. This outcome aligns closely with the results of lithological discrimination and hydrothermal alteration mapping in the study area.

The gneisses (zircon U–Pb age = 726 ± 40 Ma; Stern et al., 1989) are mainly exposed at G. Duag and G. Soaorib (Fig. 8), where they are thrust over by metaultramafic rocks along Wadi Ogdeer (Fig. 11a). The gneisses are also juxtaposed against the metavolcano-sedimentary associations and the intrusive metagabbro-diorite rocks along an intrusive contact. They show distinct gneissose and migmatite structures made up of alternating bands of quartzofeldspathic and mafic minerals. The gneissic rocks are mainly foliated in N–S and occasionally NE–SW or NW–SE directions. In some outcrops, the gneisses are folded and cut by numerous pegmatite and quartz veins that align with the foliation trends.

The ophiolitic rocks are primarily consisting of metaultramafic rocks, metagabbros, and metavolcanics that are widely exposed in the southern part of the study area. The metaultramafics are intensively sheared silica-carbonate listwaenite that occur along the Ogdeer thrust. These rocks have distinct reddish-brown cubic crystals of goethite replacing pyrite, particularly at or near their contact with the gneissic units. The ophiolitic metagabbros crop out around the Soaorib Gold Mine in the southern part of the study area. They are medium-grained and appear as circular mass in tectonic contact with the island arc metavolcano-sedimentary rocks and the ophiolitic metavolcanics (Fig. 8). The ophiolitic metavolcanics are highly foliated with numerous shear-sense indicators. They mainly crop out as NE-trending elongated sheets intercalated with the island arc metavolcano-sedimentary rocks at G. Iss, occasionally displaying pillow structure (Fig. 11b). Several NNE-SSW to NE-SW mineralized quartz veins, associated with hydrothermal alteration zones, are hosted in the ophiolitic metavolcanics (Fig. 8).

The metavolcano-sedimentary rocks include intermediate to acidic metavolcanics and volcaniclastic metasediments. They represent the most common lithological unit, as they crop out extensively from north to south throughout the study area (Fig. 8). Most of the metavolcano-sedimentary exposures occur in the central and southern parts (i.e.

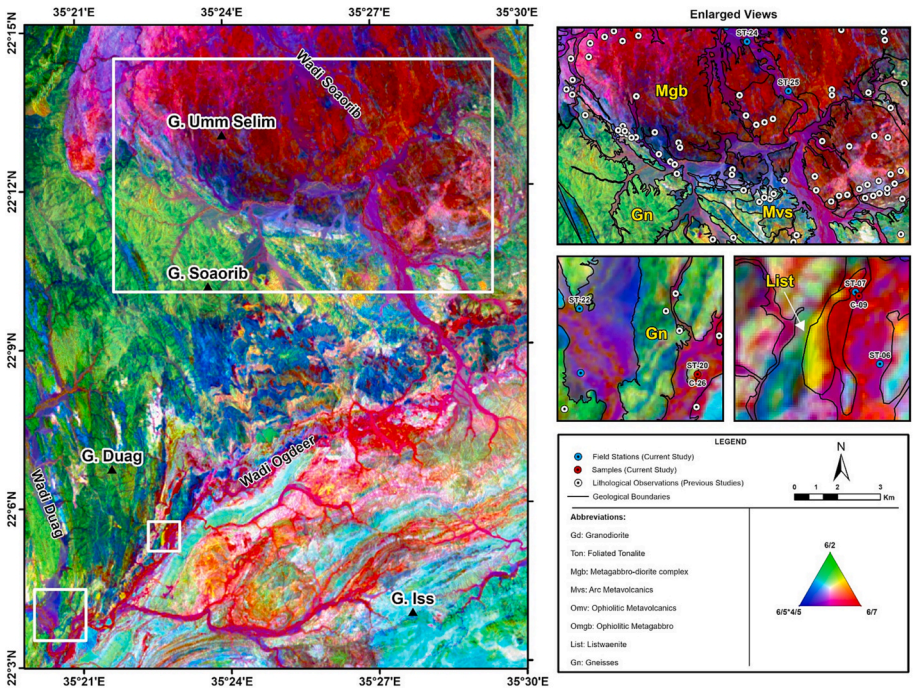


Fig. 6. Lithological discrimination using Landsat 9 band ratio composite (6/7, 6/2, 6/5 × 4/5) in RGB. Representative field stations and petrographic samples are labeled with their respective IDs to provide spatial cross-references to the field and petrographic observations presented in subsequent figures.

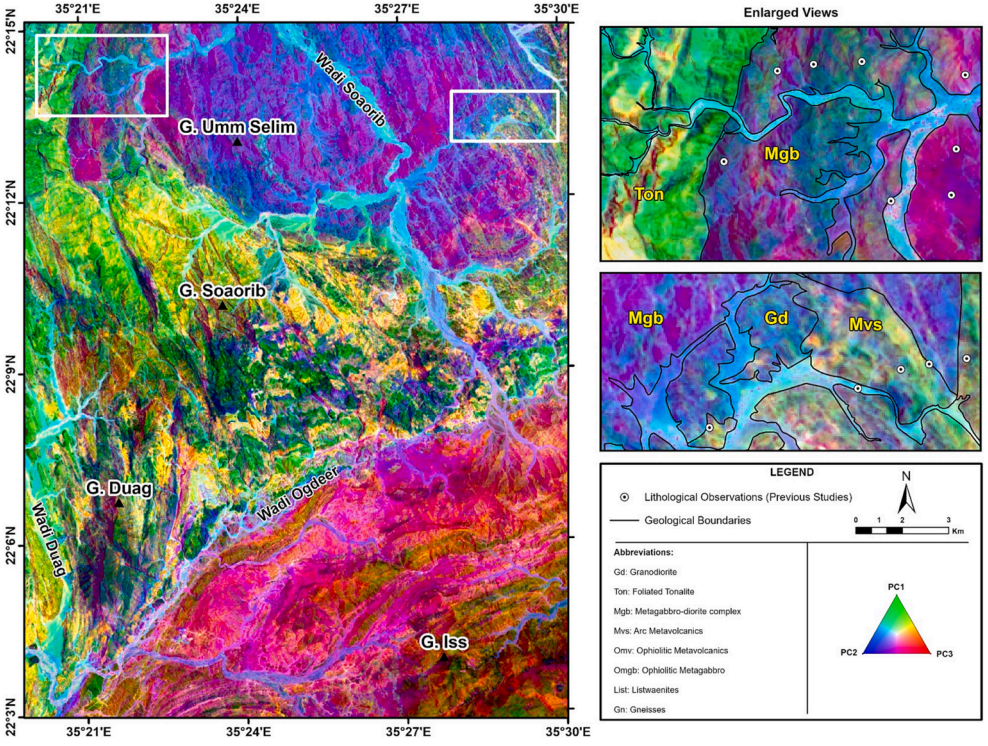


Fig. 7. Lithological discrimination using Landsat 9 principal component analysis (PCA 312) in RGB.

south of G. Soaorib and near G. Iss), although some outcrops exist in the north, forming a tectonic contact against the granitoids and gneisses, as well as intrusive contact with the metagabbro–diorite rocks (Fig. 11c).

The metagabbro–diorite complex is the second most extensive lithological unit in the study area and is mainly exposed at G. Umm Selim in the northern part (Fig. 8; 11d). The rocks in this complex display weak deformation compared to the ophiolitic metagabbro found at the Soaorib Gold Mine. They show intrusive contacts against the metavolcano-sedimentary rocks as well as the granitoids found to the east and west. The southern boundary of the metagabbro-diorite complex at G. Umm Selim is defined by a sharp intrusive contact against the gneisses of G. Soaorib. Felsic dykes are recorded cutting the metagabbro–diorite exposures, particularly near Wadi Soaorib (Fig. 11e).

The granitoid rocks occur as small outcrops of foliated tonalites and

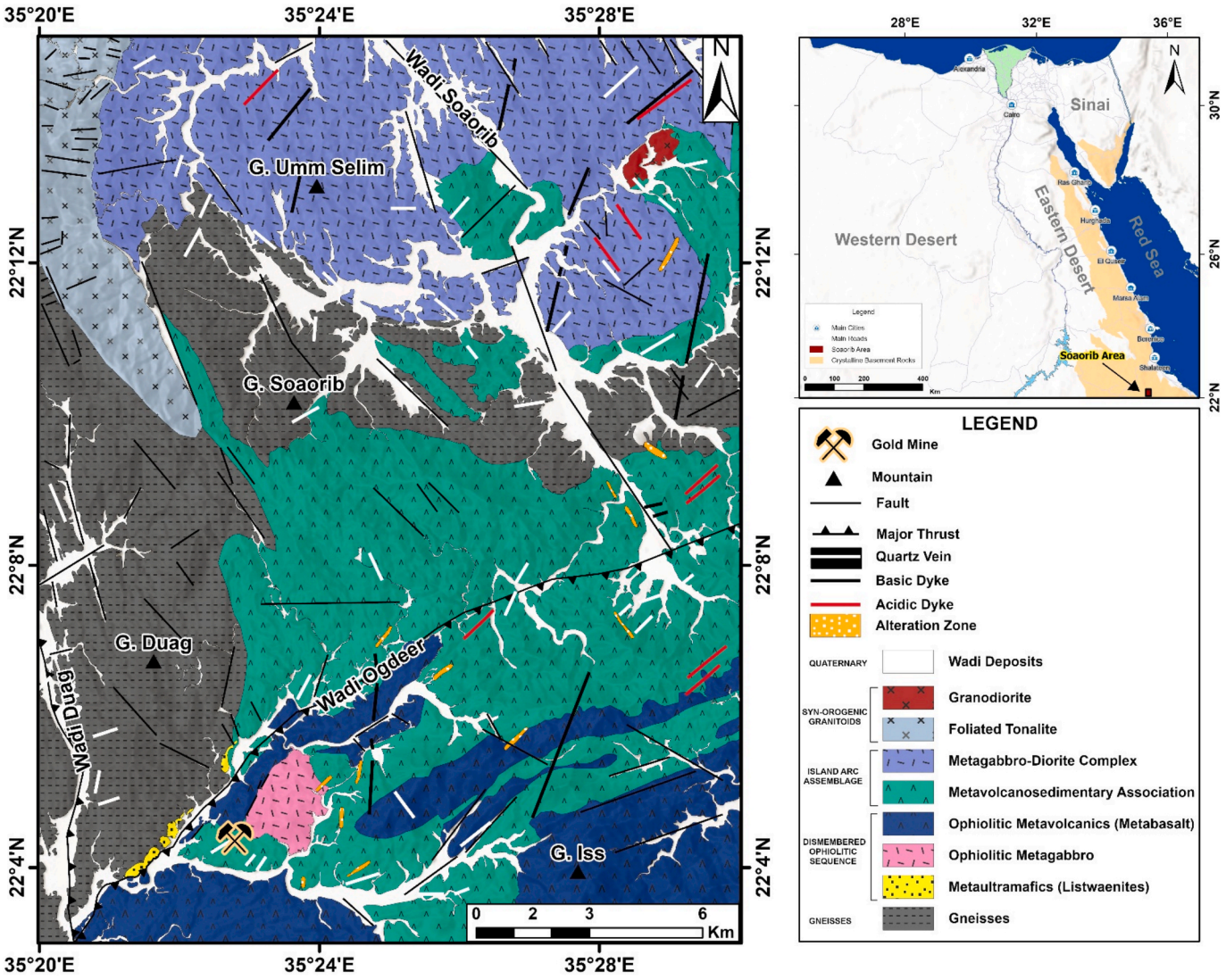


Fig. 8. Final geological map of the Soaorib area interpreted from remote sensing data and refined through field work and petrographic investigations.

granodiorites. The tonalites occur as an elongated strip separating the metagabbro-diorite complex of G. Umm Selim from the gneisses of G. Duag (Fig. 11f). The granodiorites occur in the northeastern part of the study area as a small mass, where they intrude the metavolcano-sedimentary unit and the metagabbro-diorite complex (Fig. 8).

Ancient mining activities, such as rodstone huts, grinding and milling stones, and rock scratches (Fig. 12a–c), were recorded in the Soaorib area. Additionally, the Soaorib Gold Mine is currently active (Fig. 12d), emphasizing the economic significance and continuing potential of the area as an attractive prospect for gold mineralization. The gold-lode is mainly represented by a set of auriferous quartz veins and their related hydrothermal alteration within the metavolcanic rocks. The quartz veins strike NNE-WSW to NE-SW and extend up to 200 m in length and ~1 m thick. Each vein may show little deviation in direction and sometimes suffers from branching into smaller veinlets. Based on field observations, the quartz veins are predominantly milky and smoky, massive to weakly foliated, and occasionally exhibit pinch-and-swell structures (Fig. 12e). The veins are commonly parallel or oblique to the dominant shear fabrics and are spatially associated with zones of intense shearing, brecciation, and wall rock alteration, particularly within the adjacent intermediate to acidic metavolcanics (Fig. 12f). The quartz veins are notably rich in sulphides and fracture-filling iron oxides (Fig. 12g-h). Field exposures reveal that the quartz veinlets hosted within strongly sheared metavolcanic rocks, exhibit clear shear-related deformation features (Fig. 12i).

4.5. Petrography

The petrographic results verify and support field observations and remote sensing interpretations by refining the characterization and nomenclature of the mapped rock units.

Gneisses are medium- to fine-grained quartzofeldspathic rocks. They are composed of quartz, plagioclase, hornblende, minor biotite and muscovite, as well as accessory zircon, titanite, and Fe-oxides. Quartz often forms elongated crystals with features of ductile deformation such as stretched grains with undulose extinction. Plagioclase typically forms subhedral to anhedral crystals with distorted twin lamellae as well as undulose extinction. The plagioclase and quartz show characteristic micro-textures of oriented crystals wrapped by cuspate grains of mica (Fig. 13a) or recrystallized porphyroblasts wrapped by foliation (Fig. 13b), particularly along the thrust contact with the ophiolitic rocks. Hornblende crystals are 0.2–0.5 mm long that occasionally twined and zoned. Muscovite and biotite occur as interstitial fine flakes with strong preferred orientation that define the main foliation.

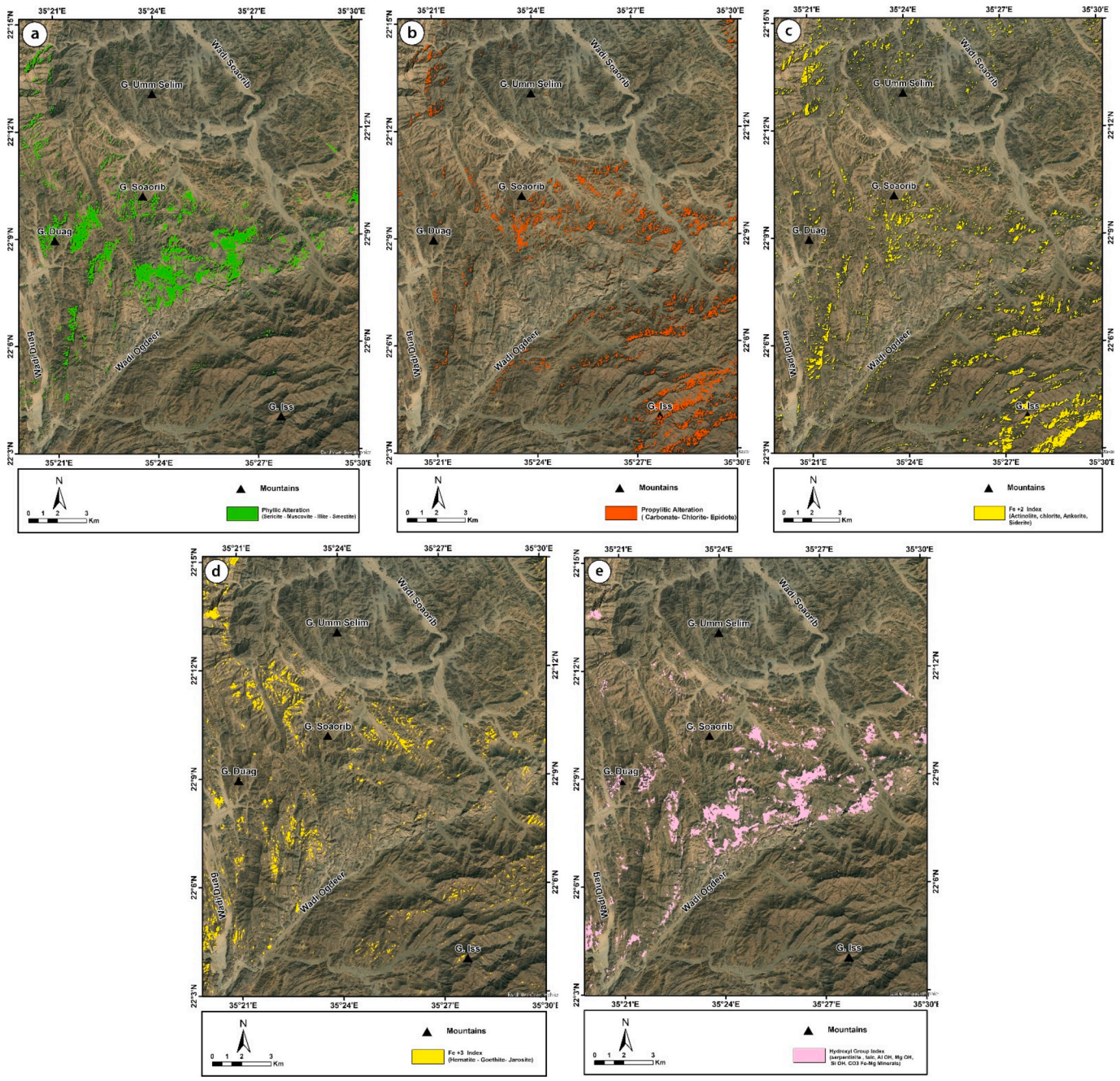


Fig. 9. Hydrothermal alteration mapping using ASTER mineral indices. (a) Phyllic alteration index. (b) Propylitic alteration index. (c) Ferrous iron (Fe^{2+}) alteration index (d) Ferric iron (Fe^{3+}) alteration index. (e) Hydroxyl (OH) group index.

The ophiolitic rocks comprise metaultramafic rocks, metabasalt, and metagabbro. The metaultramafics are mainly carbonate-silica and silica-carbonate listwaenites. The carbonate-silica listwaenite consists of ≥80 vol% carbonate minerals with minor quartz, Cr-spinel, muscovite, and few relics of serpentinite. The carbonate minerals display medium- to coarse-grained crystals as well as fine aggregates (Fig. 13c). The coarse-grained carbonates are subhedral with well-developed cleavage, which are variably deformed as indicated by kink banding and recrystallization to fine-grained aggregates. The silica-carbonate listwaenite consists of quartz, carbonate minerals, and relict serpentinite (Fig. 13d) with minor Cr-spinel and chlorite. Quartz occur either as anhedral to subhedral interlocking grains or as fine-grained vein fillings. The carbonate minerals exist as patches with different crystal sizes. Relict serpentine minerals, as protolith remnants, are clearly observed as fine-grained fibrous/platy aggregates showing mesh texture. The ophiolitic metagabbros are coarse- to medium-grained with the original igneous textures are well-preserved. They consist of plagioclase feldspar and amphibole along with secondary chlorite, epidote, calcite and accessory apatite and iron oxides. The plagioclase crystals are subhedral and are partially altered to saussurite. The amphibole appears as subhedral prismatic hornblende or fibrous uralite (Fig. 13e), showing varying degrees of alteration to chlorite and epidote, and contains fine-grained plagioclase and apatite. Some amphibole crystals enclose irregular cores of clinopyroxene (augite). The ophiolitic metabasalts are porphyritic and consist mainly of plagioclase and actinolite microphenocrysts in a groundmass of chlorite and plagioclase laths in addition to epidote and iron oxides (Fig. 13f). The plagioclase laths and crystals are affected by a mixture of saussurite whereas actinolite is a

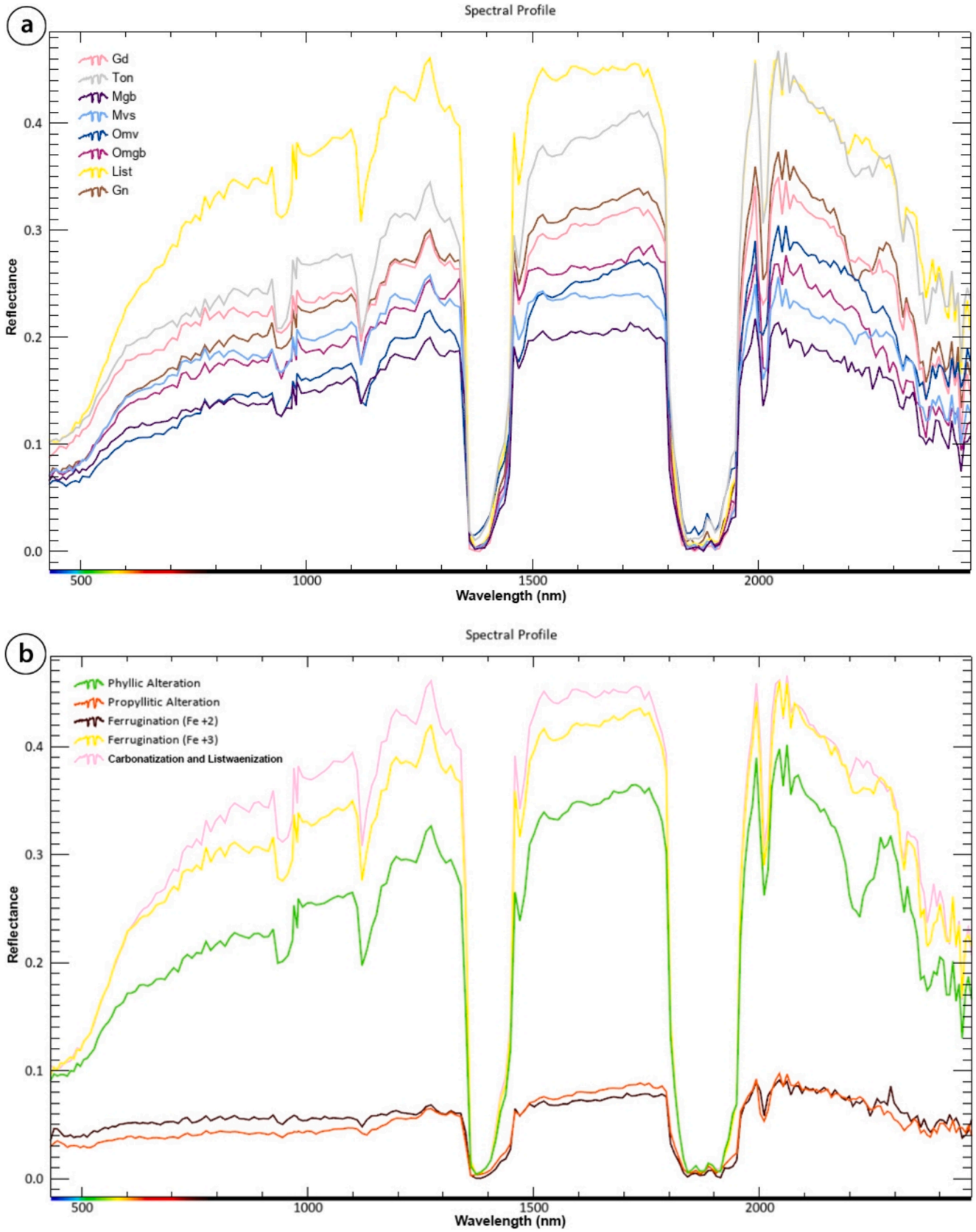


Fig. 10. Spectral reflectance curves derived from PRISMA hyperspectral analysis. (a) Spectral curves of the mapped lithological units showing variations in reflectance and absorption features. (b) Spectral curves of the main hydrothermal alteration zones highlighting diagnostic absorption features related to phyllic, propylitic, ferruginous alterations, in addition to carbonatization and listwaenization.

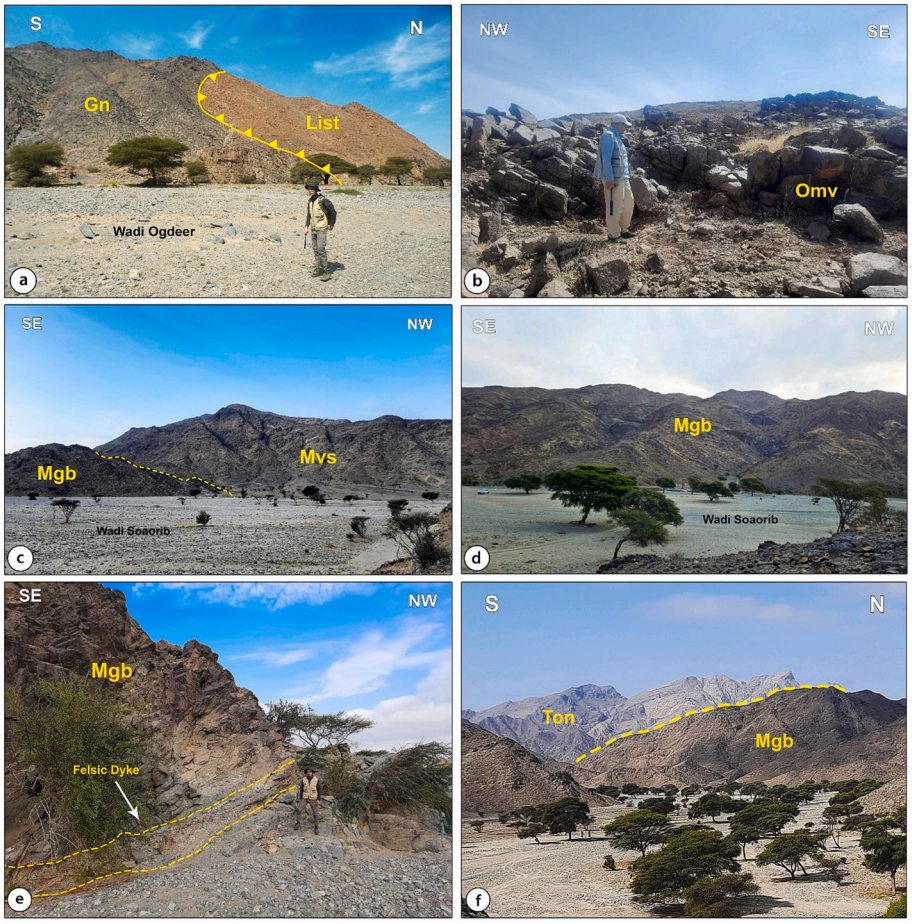


Fig. 11. Field photographs at the Soaorib area, with the corresponding field station IDs and location-reference figure numbers given in parentheses. (a) The metaultramafic rocks thrusted over the gneisses along Wadi Ogdeer (ST-03; Fig. 5). (b) Ophiolitic metabasalts with fractured and cracked pillow structure near G. Iss(ST-16; Fig. 4). (c) Intrusive contact between the metagabbro-diorite and the arc metavolcano-sedimentary rocks along Wadi Soaorib (ST-25; Fig. 6). (d) general view of G. Umm Selim metagabbro-diorite complex (ST-25; Fig. 6). (e) Felsic dyke cutting across the metagabbro-diorite exposure along Wadi Soaorib (ST-24; Fig. 6). (f) Clearly identified sharp intrusive contact separating the foliated tonalites from the metagabbro-diorite complex of G. Umm Selim (ST-24; Fig. 6). Abbreviations: Gn = Gneisses; List = Listwaenite; Omgb=Ophiolitic Metagabbro; Omv=Ophiolitic Metavolcanics; Mvs = Arc Metavolcanics; Mgb = Metagabbro-diorite complex; Ton = Tonalite; Gd = Granodiorite.

pseudomorph after the original clinopyroxene (augite). Few grains of the primary augite occur in association with actinolite.

The metavolcano-sedimentary association consists of intermediate to felsic metavolcanics and volcaniclastic metasediments. The intermediate metavolcanics are mainly porphyritic andesites with plagioclase phenocrysts in a microcrystalline groundmass (Fig. 13g). The groundmass is dominated by saussuritized laths of plagioclase, together with actinolite, chlorite, epidote and subordinate biotite and quartz. Opaque minerals, as subhedral skeletal grains, are common accessory minerals. The felsic metavolcanics are porphyritic dacite identified by phenocrysts of quartz and feldspar (plagioclase and k-feldspar) in a microcrystalline groundmass consisting of quartz, feldspars, and biotite. The volcaniclastic metasediments include metagreywacke metasiltstone, and metamudstone. The metagreywacke is characterized by poor to moderate sorting and is composed of angular, sand-sized grains of quartz, lithic fragments, and feldspars embedded within a silty matrix. In contrast, the metasiltstone exhibits a similar mineralogical assemblage, although more than 70% of its constituents are silt-sized particles. The *meta*-mudstone consists of mud-size particles of quartz, chlorite, clay minerals and Fe-oxides (Fig. 13h).

The metagabbro of the metagabbro-diorite complex is coarse-grained and consists of plagioclase, hornblende, pyroxene relics, and quartz. Secondary alterations products are chlorite, epidote, and zoisite, whereas titanite, zircon, and apatite are accessory minerals. Subhedral plagioclase crystals exhibit variable saussuritization. Hornblende is partially altered to pale green chlorite, calcite, and epidote. The metadiorite is composed of plagioclase feldspar, hornblende, quartz, and biotite, with minor secondary chlorite, epidote and sericite. Apatite, zircon, titanite, and opaques are accessory minerals. The plagioclase is often partially or completely saussuritized. Quartz shows wavy extinction and grain boundary migration as signs of deformation.

Intense hydrothermal alterations, with alteration halos varying in size from few meters to ~20 m, highly affect the metavolcanics surrounding the quartz veins. On the basis of their distance from quartz veins, they can be classified into distal (propylitic) and proximal (phyllic) alteration zones in addition to late carbonatization and ferrugination. Propylitic alteration affecting the intermediate and basic metavolcanics is revealed by the widespread replacement of the primary mafic minerals with chlorite and epidote, which partly obscure the original magmatic textures. Chlorite and epidote occur as fibrous and fine-grained aggregates while feldspars are commonly altered to varying degrees (Fig. 14a). Minor opaque phases, together with sporadic epidote and carbonate, occur along fractures and open spaces. These findings suggest a low-temperature hydrothermal alteration, typically associated with the outer or distal zones of the mineralized systems. Phyllic alteration affecting the acidic metavolcanics is defined by pervasive replacement of the feldspars by fine-grained sericite aggregates, typically aligned along cleavage planes. Quartz remains largely unaltered

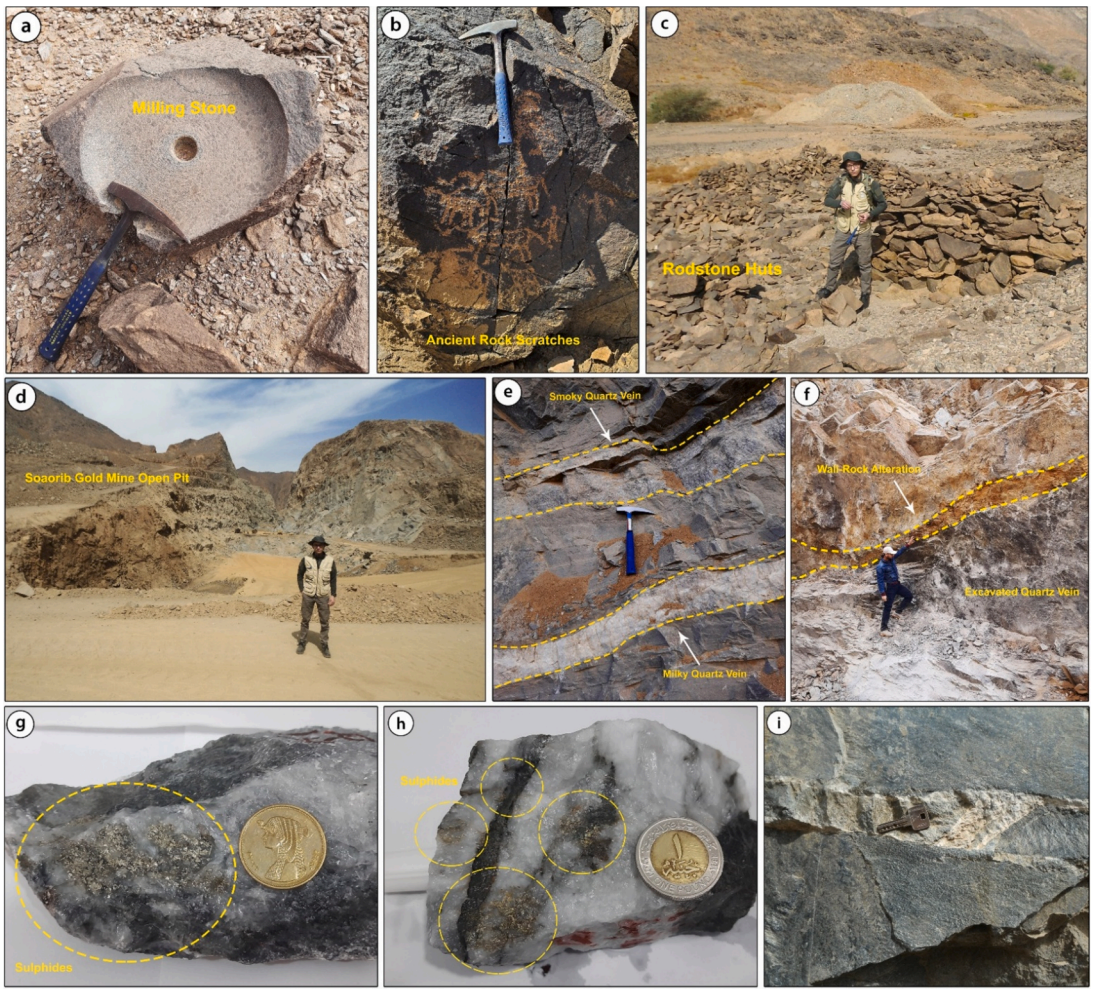


Fig. 12. Representative field photographs illustrating ore morphology, mineralization style, and evidence of historical mining at the Soaorib Gold Mine, with the corresponding field station IDs and location-reference figure numbers given in parentheses. (a) Ancient milling stone indicating historical gold processing (ST-01; Fig. 5). (b) Rock scratches and surface markings related to ancient mining activities (ST-01; Fig. 5). (c) Remains of rodstone huts constructed by earlier miners (ST-01; Fig. 5). (d) General view of the active Soaorib open-pit mine (ST-02; Fig. 5). (e) Two parallel NNE-SSW trending quartz veins (one is smoky and other is milky) with pinch-and-swell structures (ST-02; Fig. 5). (f) Carbonaceous wall-rock alteration around excavated quartz vein hosted in highly altered basic metavolcanics (ST-02; Fig. 5). (g–h) Hand specimens of milky to smoky quartz veins rich in sulphide minerals and iron oxides (ST-02; Fig. 5). (i) Quartz veinlet cutting sheared metavolcanics (ST-02; Fig. 5).

with clear anhedral grains. The plagioclase laths are strongly altered with partially obliterated twin lamellae (Fig. 14b). Minor opaque minerals and disseminated iron oxides are also present within the groundmass. Carbonatization is identified in two distinct forms. The first one is carbonate veining (Fig. 14c), where coarse calcite ± dolomite crystals occupy microfractures cutting across the foliation. The second is carbonate replacement in the host rock (Fig. 14d), where carbonates extensively replace feldspar and mafic minerals. The altered groundmass is also composed of chlorite, minor sericite, and opaque minerals. Both forms indicate circulation of CO_2-rich hydrothermal fluids, representing a late-stage alteration event along structural conduits such as shear zones. Ferrugination is mainly represented by the development of secondary iron oxides along fractures and open spaces, commonly associated with late-stage fluid circulation. Although ferruginous alteration was not observed as a distinct pervasive alteration zone in the studied thin sections, iron oxides occur as pervasive fracture-filling and disseminated phases within the altered groundmass, indicating localized oxidation processes along structural pathways.

4.6. Structural analysis and mapping

Results of the automatic lineament extraction and density-based mapping yielded a set of insights regarding the structural framework, lithology, alteration zones, as well as recent mining activities in the study area (Fig. 15). From a structural perspective, the analyses revealed a prevailing NE–SW to ENE-WSW structural trend, along with subordinate N-S, NNW, NNE and E–W to ENE trends. Density-based mapping of the extracted lineaments highlighted zones of high densities, that spatially correlate with alteration and high strain zones associated with major fault systems (i.e. Ogdeer thrust fault). Gneisses and metavolcanics are the most deformed lithological units throughout the study area. Additionally, the alteration zones are structurally influenced by these lineaments, with spectral anomalies usually identified at the intersections of areas with high lineament densities. The Soaorib Gold Mine lies in an area with a high density of lineaments, where hydrothermal fluids have infiltrated into fractures, joints and fault planes leading to the deposition of gold and sulphides.

A sharp intrusive contact is precisely traced in the northwestern corner of the area using the FCC-753 in RGB (saturation stretched) as well as the PCA-423 in RGB (Fig. 16a and b). Near the entrance of the Soaorib Gold Mine at Wadi Ogdeer, the area shows significant deformation caused by two dominant structural trends, which are: (1) The N–S Hamisana trend that primarily governs the western sector, affecting the G. Duag gneisses and the thrust-faulted listwaenite sheets; (2) the

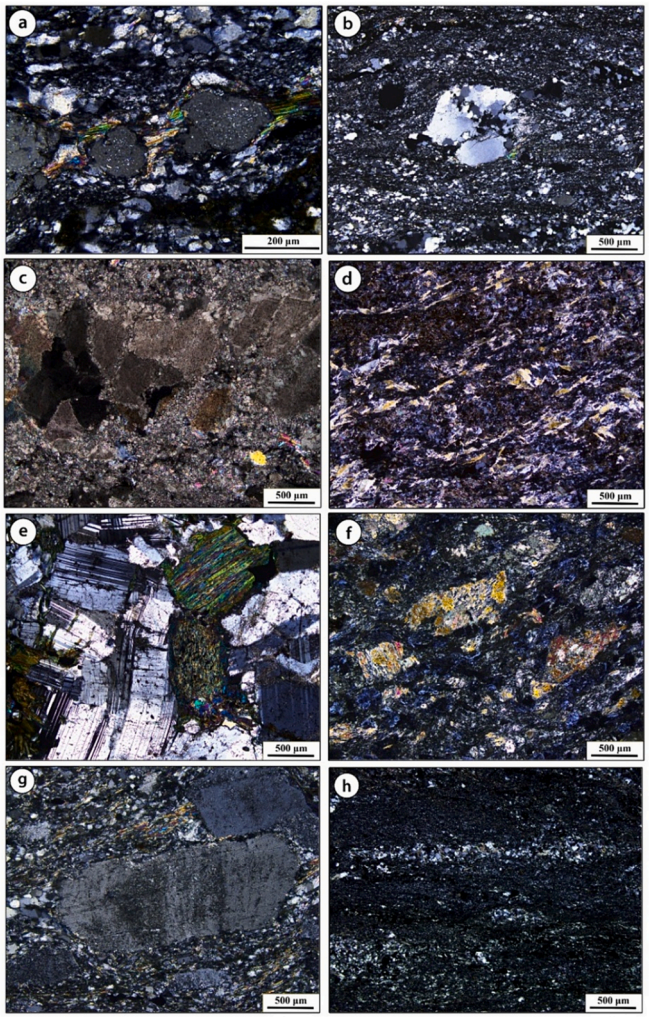


Fig. 13. Photomicrographs, in crossed polarized light (XPL), of the Precambrian rocks in the Soaorib area, with the corresponding sample IDs and location-reference figure numbers given in parentheses. (a) Elongated cuspate grains of mica around oriented plagioclase porphyroblasts in the gneiss (C-26; Fig. 6). (b) Quartz porphyroblast wrapped by foliation in the gneiss showing recrystallized grains and undulose extinction (C-26; Fig. 6). (c) Carbonate listwaenite showing the carbonate minerals as medium- to coarse-grained crystals and as fine aggregates (C-09; Fig. 5). (d) Silica-carbonate listwaenite showing quartz as anhedral interlocking grains and relict serpentinite as fine-grained patches (C-02; Fig. 5). (e) Ophiolitic metagabbro consisting of plagioclase with deformed twin lamellae and uralitized amphibole (C-33; Fig. 5). (f) Ophiolitic metabasalt with porphyritic texture consisting of saussuritized plagioclase and actinolite microphenocrysts in a microcrystalline groundmass (C-05; Fig. 5). (g) Arc metavolcanics (*meta*-andesite) with plagioclase phenocrysts in a microcrystalline groundmass consisting of plagioclase, actinolite, epidote, and chlorite (C-19; Fig. 5). (h) Metamudstone consisting of mud-size laminae consisting of quartz and chlorite with minor intercalations of metasiltstone (C-10; Fig. 5).

Onib–Sol Hamed trend that affects the eastern part. The intervening zone comprises intensely sheared ophiolitic rocks (Omv and Omgb) that host the Soaorib Gold Mine (Fig. 16c–d). Using two FCC-753 composites (one saturation-stretched and the other decorrelation-stretched), two distinct dextral strike-slip faults trending NW–SE are clearly observed truncating the ophiolitic metavolcanics near G. Iss (Fig. 16e–f).

An updated structural framework was established by combining existing structural maps with satellite-derived lineaments and field observations. The resulting framework clarifies the distribution and orientation of major faults, folds, and shearing-related structures, that shows enhanced continuity and spatial relationships of regional structural elements (Fig. 17a). This integration established coherence between current geological knowledge and remote-sensing observations, providing a robust basis for subsequent structural analysis and interpretation of the deformation phases. Stereographic projections of field measurements reveal distinct orientation clusters related to different deformation-related structural fabrics (Fig. 17b–f).

4.7. *Gold potentiality mapping (GPM)*

The generated GPM classified the study area into five potentiality classes: Very Low, Low, Moderate, High, and Very High (Fig. 18). The spatial distribution of these classes shows a close correspondence with the geological and structural framework of the Soaorib area. In the southern part, the High and Very High classes are mainly distributed within a narrow NE–SW-trending belt extending along Wadi Ogdeer, particularly near the contact between the metavolcanic and metagabbro lithologies. The Very High class occurs as discontinuous patches embedded within broader High potentiality zones. Furthermore, the Soaorib Gold Mine is located within the High class, suggesting that this area represents the greatest spatial convergence of the favorable lithological and structural controls, highlighting Wadi Ogdeer as the most prospective sector within the study area. In contrast, the northern part, including the surroundings of G. Soaorib, G. Umm Selim, and Wadi Soaorib, is largely characterized by Very Low to Moderate classes. The Moderate and Low classes may represent areas in which only part of the favorable lithostructural controls are present and therefore may serve as secondary exploration targets that require further detailed investigation. Finally, the Very Low class is considered the least prospective within the study area.

5. Data integration and validation for the GPM

The GPM was validated against independent validation points representing direct evidence of gold mineralization, including the Soaorib Gold Mine, positive gold assay locations, quartz veins, hydrothermal alteration zones, mineralized field stations, and rodstone huts. Visual inspection indicates a clear spatial association between the independent validation datasets and the High and Very High potentiality zones of the generated GPM (Fig. 19a) in the southwestern part of the study area. The quantitative validation results are listed in Table 5 and Fig. 19a–d, which compare the spatial extent of each potentiality class with the distribution of the independent validation points. The Very High and High classes occupy only 0.71% and 5.87% of the modeled area, respectively, representing a combined area of 6.58% (Fig. 19c). Despite their limited spatial extent, these two classes contain 8% and 19% of the independent validation points, respectively, accounting for a combined 27% of all independent validation points (Fig. 19c–d and Table 5).

To evaluate the overall performance of the model, the class-specific percentages were subsequently converted into cumulative area and cumulative validation percentages (Table 5), which were then used to construct the success-rate curve (Fig. 19b). This curve is a widely adopted approach for evaluating the performance of mineral prospectivity models (Chung and Fabbri, 2003; Carranza and Laborte, 2015; Harris et al., 2025). The diagonal (1:1) line represents a random spatial distribution of the validation data. A success rate curve located well above the diagonal line with a steep initial slope indicates high predictive performance, whereas a curve approaching the diagonal line indicates prediction close to random. The success-rate curve shows that 72.03% of the cumulative validation points are captured within only 36.80% of the modeled area, demonstrating that the model effectively delineates areas where mineralization-related features are concentrated. The model performance was further evaluated using the Enrichment Ratio (ER), which measures the concentration of independent validation points within the identified favorable zones relative to that expected under a random spatial distribution (Chung and Fabbri, 2003; Carranza, 2009). The ER was calculated for the combined High and Very High

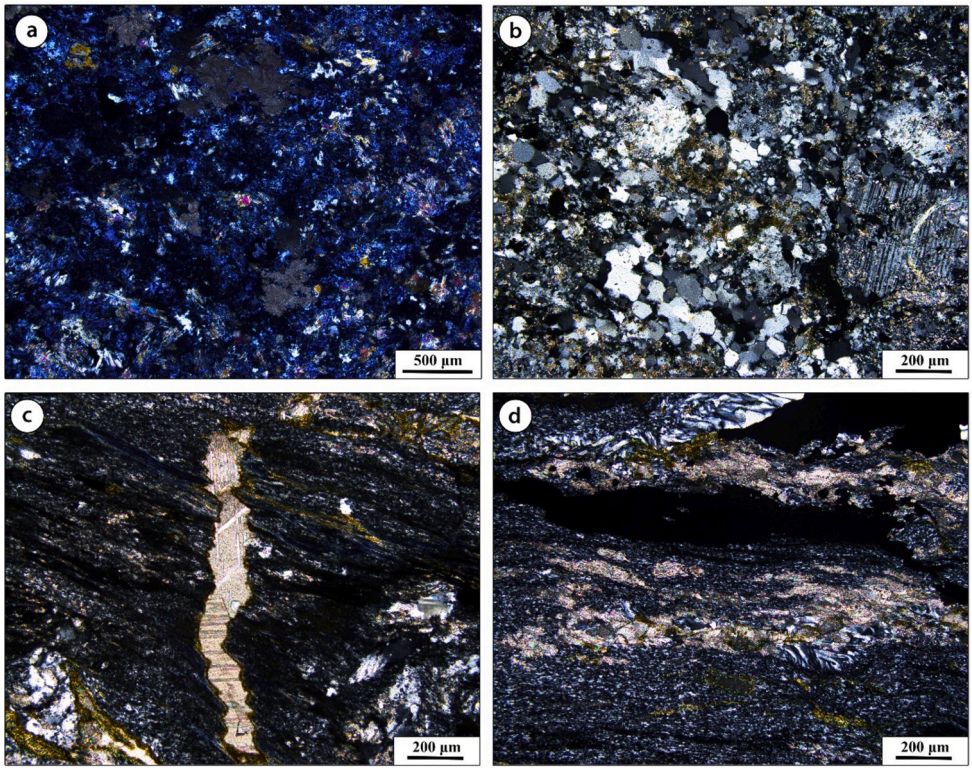


Fig. 14. Photomicrographs, in crossed polarized light (XPL), of the alteration zones at the Soaorib Gold Mine, with the corresponding sample IDs given in parentheses and their locations shown in Fig. 5. (a) Chloritization (propylitic alteration) represented by replacement of mafic minerals by chlorite aggregates (A-50). (b) Sericitization (phyllic alteration) where the plagioclase is partially or completely replaced by fine-grained sericite (A-51). (c) Calcite veinlets crosscutting foliation planes (A-52). (d) Carbonate minerals replacing the host rocks along interstitial spaces (A-52).

potentiality classes, as these represent the priority exploration targets:

$$ER = \frac{\%\ \text{Cumulative Validation}}{\%\ \text{Cumulative Area}}$$

The calculated ER value of 4.11 (ER > 1) indicates that independent validation points are concentrated more than fourfold within the identified favorable zones compared to a random distribution, further demonstrating the ability of the model to prioritize the most prospective areas for gold exploration. (Fig. 19c and d).

6. Discussion

6.1. Tectonic emplacement of orogenic gold deposits in the Egyptian Segment

Orogenic gold deposits (lode or mesothermal) are widely distributed in the CED and SED, which host the majority of highly potential gold localities and mines. In general, these deposits are formed at convergent plate boundaries and often located within metamorphosed terranes in the form of hydrothermal quartz ± carbonate(s) veins or disseminated gold in the Neoproterozoic rocks. These systems exhibit close spatio-temporal relationships to syn- and post-deformation patterns (compressional to transpressional). The hydrothermal fluids traditionally track the rock fractures and lineaments that act as pathways and traps for migration of mineralized fluids, leaving remarkable alteration zones. Several independent studies have demonstrated that gold mineralization in Egypt is preferentially associated with late transpressional shear zones, where strain localization during oblique convergence promoted hydrothermal fluid flow, quartz vein emplacement, and gold deposition (Groves et al., 1998; Zoheir, 2012a; Zoheir and Klemm, 2007; Goldfarb et al., 2001).

Abd El Monsef (2025) mentioned that the ANS has two tectonic orogens resulted in recognizable suture zones, as follows; (1) An early Ocean-Ocean collisional event (~850–650 Ma); including subduction of oceanic crust beneath island arcs to produce accretionary volcanic arcs and ophiolites. This convergent motion was responsible for E/ENE tectonic orientation (e.g. Allaqi-Heiani-Sol Hamed sutures (730–706 Ma, Ali et al., 2010), and (2) A second Arc-Continent collision (~635–540 Ma); involved in formation of syn- to late- granitic series and their equivalent Dohkan volcanics. It is represented by the NNW–SSE Najd Fault System (NFS) and N-S Hamisana Shear Zone (620–560 Ma; Stern, 1985). Multiple geologic and radiogenic evidence correspond the formation of orogenic gold in Egypt to the second stage of orogeny and related post-orogenic convergence/transpression tectonism (Zoheir et al., 2019; El Aref et al., 2020). However, some studies support the idea of two tectonic stages for gold formation in SED consistent with the previously described two tectonic orogens (Botros, 2015; El Hebiry, 2021).

6.2. Deformation history in the Soaorib area

The SED shows a complex deformation history related to the Neoproterozoic tectonic evolution of the ANS, beginning with an early stage of island arc accretion, followed by crustal shortening (transitioning from a purely compressional to a transpressional regime), and culminated with late-stage brittle extension (Johnson et al., 2011; Abdeen and Abdelghaffar, 2011; Kusky and Ramadan, 2002). This progressive evolution resulted in thrust faults, folding, shear zones, and brittle structures that collectively governed the regional structural framework of the ESD and played a key role in fluid movement and gold deposition (Zoheir, 2008; Groves et al., 1998; Zoheir and Klemm, 2007; Goldfarb et al., 2001). Detailed field investigation and structural analyses of the Soaorib area reveal the occurrence of three main regional deformation phases (D1–D3). The earliest deformation phase (D1) corresponds to

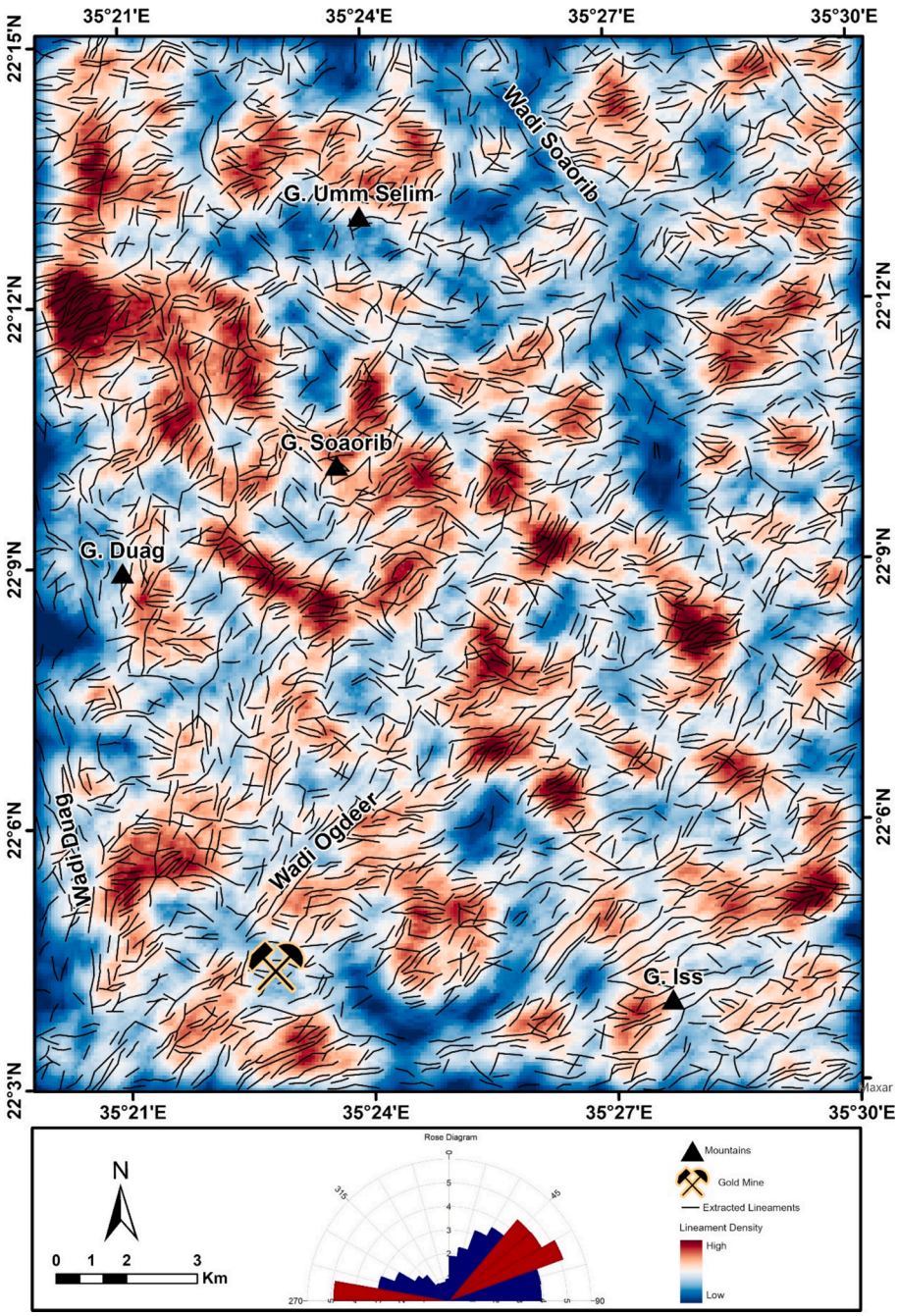


Fig. 15. Automatic lineament extraction from Sentinel-2 PC1 imagery showing extracted lineaments overlaid on a lineament density map, highlighting zones of high and low lineament concentrations. The accompanying rose diagram illustrates the dominant NE–SW structural trend.

N–S–oriented arc accretion and terrane amalgamation involving the Gerf terrane in the SED and the Gabgaba/Gebeit terranes in northern Sudan, leading to the development of the Allaqi–Heiani–Onib–Sol Hamed suture (Kusky and Ramadan, 2002; Zoheir, 2012b; Abdeen and Abdelghaffar, 2011; Zoheir and Klemm, 2007). This phase was marked by ductile deformation and resulted in the development of an early ENE and WNW regional penetrative planar fabric (S1) (Fig. 17b–c), regionally developed thrust contacts (T1), such as the Ogdeer thrust, and associated F1 folding (Fig. 20a). The occurrence of fold interference patterns with southwest-plunging fold axes suggest multiple folding events that reflect polyphase ductile deformation and progressive reorientation of the regional stress field during terrane accretion (Zoheir and Klemm, 2007) (Fig. 20b). While this phase played a fundamental role in shaping the crustal architecture, it was not directly associated with gold mineralization (Zoheir, 2012a).

The second phase of deformation (D2) signifies the collision stage between East and West Gondwana and occurred under a prevailing E–W compressional tectonic regime (Abdeen and Abdelghaffar, 2011; Kusky and Ramadan, 2002; Johnson et al., 2011). Deformation during this phase caused additional increasing and reworking of the earlier ductile fabrics, leading to the development of a second NNE to NNW penetrative planar fabric (S2) (Fig. 17d;20c), T2 thrust faults striking NNE to NNW such as the Duag thrust that controls the contact between the different rock units, together with related F2 folding featuring NE–SW–trending axial traces (Fig. 8; 16a-d; 17). Thrust sheets with the same trend are also observed in different rock units (Fig. 20d). The structural characteristics of the D2 phase indicate progressive reorientation of the regional stress field during the collision between East and West Gondwana (Johnson

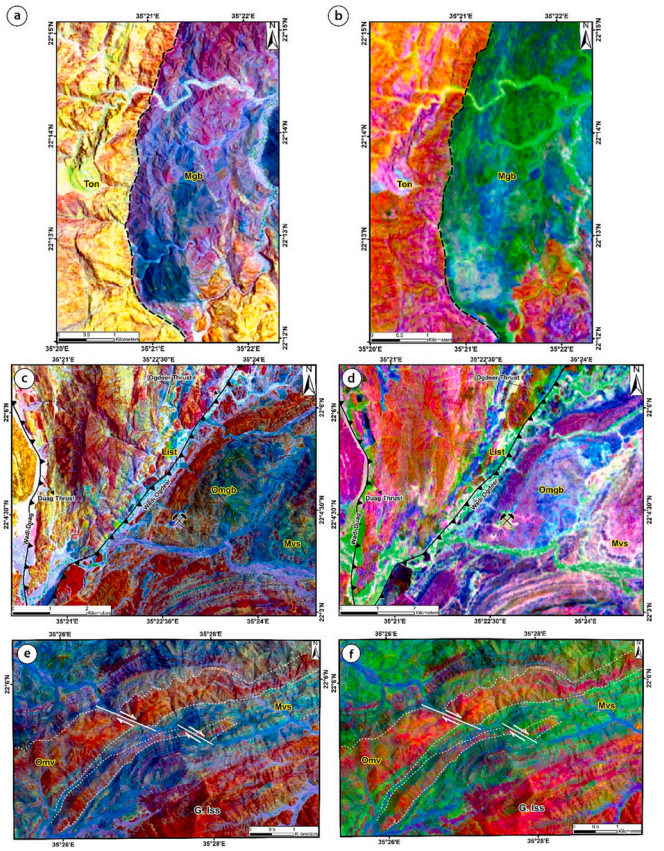


Fig. 16. (a) Landsat-9 FCC-753 in RGB (saturation-stretched) and (b) PCA-423 in RGB showing the clearly defined intrusive contact in the northwestern part of the study area. (c) Landsat 9 FCC-753 in RGB (saturation-stretched) and (d) Landsat 9 PCA-423 in RGB showing the structural complexity near the entrance of Wadi Ogdeer. The area is strongly deformed by the N–S Hamisana trend to the west, which gradually bends eastward into NE–SW belts aligned with the Onib–Sol Hamed trend. A highly sheared ophiolitic exposure (Omv and Omgb) lies between the two trends and hosts the Soaorib Gold Mine. (e) Landsat 9 FCC-753 in RGB (saturation-stretched) and (f) Landsat 9 FCC-753 in RGB (decorrelation-stretched) showing two dextral strike-slip faults truncating the ophiolitic metavolcanics near G. Iss at the southern margin of the study area; abbreviations as in Fig. 11.

et al., 2011) and mark the culmination of regionally distributed compressional deformation. This phase represents a transitional stage preceding the shift toward the transpressional, shear-dominated deformation that characterized the subsequent D3 phase (Zoheir, 2012a).

The third phase of deformation (D3) represents a fundamental shift in the deformational style from compression to transpression caused by continuing oblique convergence between East and West Gondwana. During this stage of deformation, strain became highly localized and shear-dominated within major shear zones affected by the NFS; 650–600 Ma (Stern et al., 1989; Greiling, 1987; de Wall et al., 2001; Johnson et al., 2011; Abdeen and Abdelghaffar, 2011; Zoheir, 2012b; Zoheir and Klemm, 2007; Kusky and Ramadan, 2002). Deformation during this phase was directly related to the Hamisana shear zone (HSZ) and its related subsidiary shear zones, predominantly trending NNE to NNW within, where rocks experienced intense strain localization and attained peak metamorphic conditions (Zoheir, 2012a; Kusky and Ramadan, 2002; Stern et al., 1989; Miller and Dixon, 1992; de Wall et al., 2001). Due to the combined effects of transpressional shearing, the D3 deformation phase is marked by the development of two distinct types of NNE to NNW S3 foliation: (i) a well-developed shear foliation spatially restricted to shear zones (Fig. 17e; 20e-f), and (ii) a locally preserved crenulation foliation, especially noted in gneissic rocks (Fig. 17e; 21a). Both types of S3 foliation are clearly distinct from the earlier regional penetrative foliations (S1 and S2). The D3-related structures include positive flower structures (Fig. 21b) that confirm the transpressional nature of deformation. Intensive strain is clearly recorded in the quartz veins and their hosting lithologies (Fig. 21c–d). During the D3 phase, well-developed top to north kinematic indicators, such as σ-type porphyroclasts, S–C fabrics, and other field-scale shear-sense indicators were observed (Fig. 21e–f). The D3 phase is also marked by the development of NW–SE–trending dextral strike-slip shear zones observed on satellite imageries (e.g. near G. Iss) (Fig. 16e–f), consistent with regional Najd-related transpressional tectonics (Zoheir, 2012a). The D3 phase is subsequently succeeded by post-orogenic deformation linked to Red Sea–related tectonics, which occurred under a transtensional regime with minor brittle overprint (Zoheir, 2012b; Bosworth et al., 2005).

6.3. *Structural controls of gold mineralization in the Soaorib area*

The auriferous quartz veins within the SED generally show close spatiotemporal association with shear zones (Zoheir, 2008, 2011; Kusky and Ramadan, 2002). Several independent studies have demonstrated that gold mineralization is primarily linked to late transpressional shear zones, where strain localization during oblique convergence promoted hydrothermal fluid flow, quartz vein emplacement, and gold deposition (Groves et al., 1998; Zoheir, 2012a; Zoheir and Klemm, 2007; Goldfarb et al., 2001). In the Soaorib area, both structural and field relationships indicate that gold distribution is structurally controlled and is temporally linked to D3 transpressional deformation. During the D3 phase, the combined effects of shear and compression facilitated the development of permeable shear-related fractures and dilation sites that acted as conduits for hydrothermal fluids (Zoheir, 2012a). Gold precipitation took place within smoky and milky quartz veins hosted in highly sheared and intensely altered metavolcanics, accompanied by extensive hydrothermal alteration and leaching of the pre-existing mafic–ultramafic assemblages. The presence of vertically developed shear foliation within listwaenites (Fig. 20e), formed through hydrothermal alteration of mafic and ultramafic protoliths, further supports *syn*-D3 hydrothermal activity. Additionally, the mineralized quartz veins often display intensive deformation features, including shearing, brecciation, pinch and swell structures, and boudinage, and are locally associated with positive flower structures (Fig. 12e–i; 21b–d), which collectively indicate formation under a transpressional regime. The consistent NNE strike and ESE dip of the quartz veins (Fig. 17f) are consistent with the dominant structural trends of the D3 shear system. These observations strongly suggests that the structural trends of the mineralized quartz veins represent subsidiary splays branching from the Hamisana shear zone, rather than being genetically related to the Onib–Sol Hamed suture (Zoheir, 2012a). This interpretation agrees with earlier studies on regional models from the SED, particularly at Romite gold deposit, located along the northeastern extension of the Soaorib area, where gold mineralization is localized within splays of the Hamisana shear zone created simultaneously with the Najd-related transpressional deformation (Zoheir, 2012b; Mesbah et al., 2026). The occurrence of boudinage, brecciation, pinch-and-swell structures, intensive shearing, and NNE-trending quartz veins at the Soaorib area reflects the structural style reported from the Romite area, reinforcing the proposed D3 transpressional model.

A comparison between the trend analysis and the structural control of gold mineralization reveals an important difference. Despite the dominant NE–ENE structural trend corresponding to the D1 phase (Fig. 15), field observations demonstrate that gold mineralization is spatially confined to the D3-related structures, particularly shear and crenulation foliations. This illustrates a key distinction between the concept of a “dominant structural trend” and that of “structural control of gold mineralization”. The dominant regional trend reflects the deformation phase with the greatest spatial extent, whereas

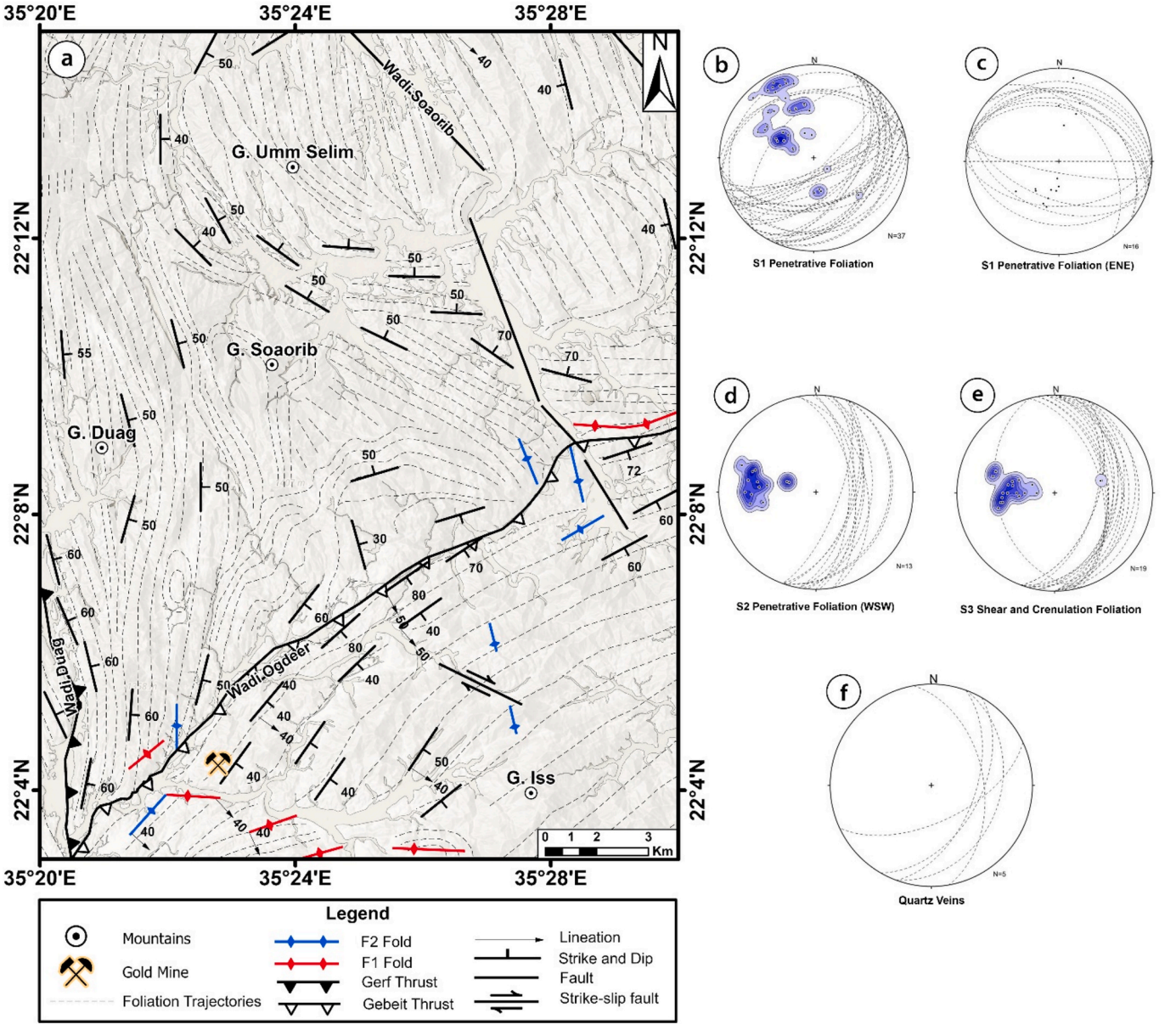


Fig. 17. Structural map and stereographic projections of field measurements from the study illustrating the orientations of structures associated with deformation phases. (a) Structural map constructed by integrating previously published structural data (e.g. Makhlouf, 2008) with satellite-derived interpretation and field-based structural mapping, showing the distribution of major thrusts, folds, shear zones, and fault systems. (b-c) Stereographic projections of S1 penetrative foliation. (d) Stereographic projection of S2 penetrative foliation. (e) Stereographic projection of S3 shear and crenulation foliation. (f) Stereographic projection of quartz veins.

mineralization is controlled by localized, high-strain structures that served as effective pathways for hydrothermal solutions. Thus, the activity of the Hamisana shear zone during D3 played a critical role in hydrothermal leaching and gold deposition without significant overprinting the pre-existing regional structural framework that was established during D1. This distinction is consistent with global orogenic gold models, where mineralization is preferentially localized within late, high-strain shear-zone splays that direct hydrothermal fluid movement, rather than simply reflecting the dominant regional structural grain (Goldfarb et al., 2001). Similar relationships are documented in the CED and SED, where gold mineralization is commonly concentrated within Najd-related transpressional shear zones and their subsidiary splays, even when the regional structural pattern is dominated by earlier accretionary fabrics (Zoheir, 2008, 2012b; Zoheir et al., 2019).

6.4. Gold potentiality mapping (GPM): scope and applicability

The ability of the generated GPM to delineate prospective zones can be attributed to the integration of the principal lithostructural controls governing gold mineralization in the Soaorib area. Thus, it should be interpreted as a regional-scale exploration model intended to highlight areas with relatively higher potential for gold mineralization based on the regional lithostructural framework and the available data. Consequently, the identified prospectivity classes should be regarded as a preliminary exploration framework rather than a direct measure of gold grade, resource potential, or economic viability. Nevertheless, they provide a valuable basis for prioritizing target areas, guiding subsequent field investigations, and optimizing future exploration efforts. Such evaluations require detailed exploration programs, including geological mapping, geochemical and geophysical surveys, trenching, drilling, and subsequent orebody modeling and resource estimation. Accordingly, the primary role of the generated GPM lies in reducing the exploration

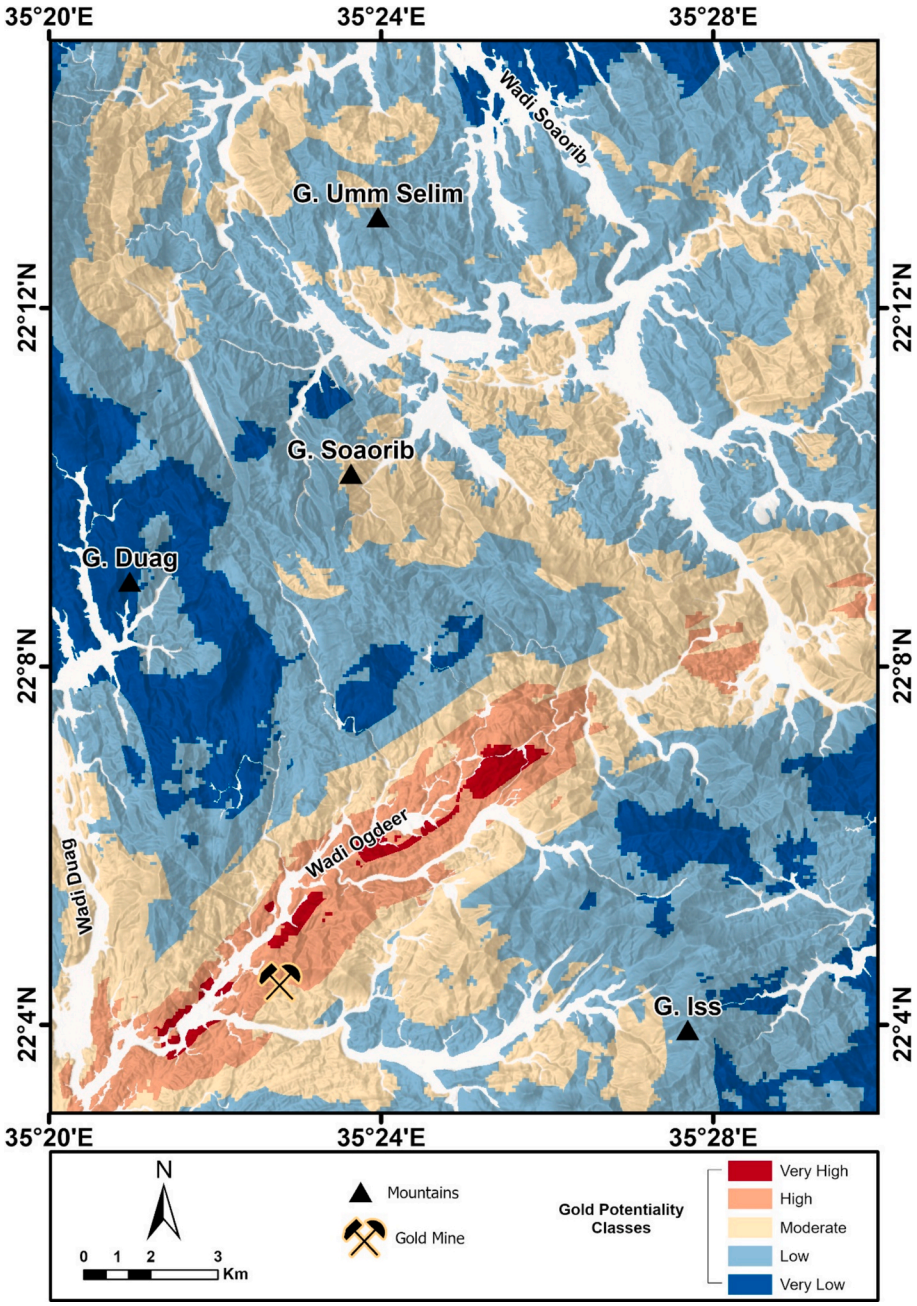


Fig. 18. The generated Gold Potentiality Map (GPM) of the Soaorib area showing the spatial distribution of gold prospectivity classified into five categories: very high, high, moderate, low, and very low.

search space and supporting decision-making by identifying priority targets for follow-up investigations rather than serving as a substitute for detailed mineral resource evaluation.

7. Conclusions

This study employs a multi-method strategy that integrates multi-sensor remote sensing data, field and petrographic studies, as well as structural analysis, which significantly improves our understanding of the geological framework and gold prospectivity for the Soaorib area in the SED of Egypt. The main conclusions are summarized as follows:

1) Lithological mapping, utilizing multisource satellite datasets and reinforced by thorough field and petrographic studies, produced a new geological map displaying four principal rock units: gneisses, dismembered ophiolitic sequence, island arc assemblages, and *syn*-orogenic granitoids.
2) Hydrothermal alteration mapping has identified the primary phyllic, propylitic, carbonatization, and ferrugination alteration zones, which shoe a notable spatial correlation with major shear zones and reactivated structural corridors, emphasizing their genetic link to structurally controlled fluid flow.
3) The study area records a polyphase deformation history involving arc accretion and terrane amalgamation between the Gerf terrane in the SED and the Gabgaba/Gebeit arc terranes in northern Sudan (D1), continental collision between East and West Gondwana (D2), and a subsequent Najd-related transpressional phase synchronous with the Hamisana shear zone activity (D3), followed by minor late brittle overprinting.

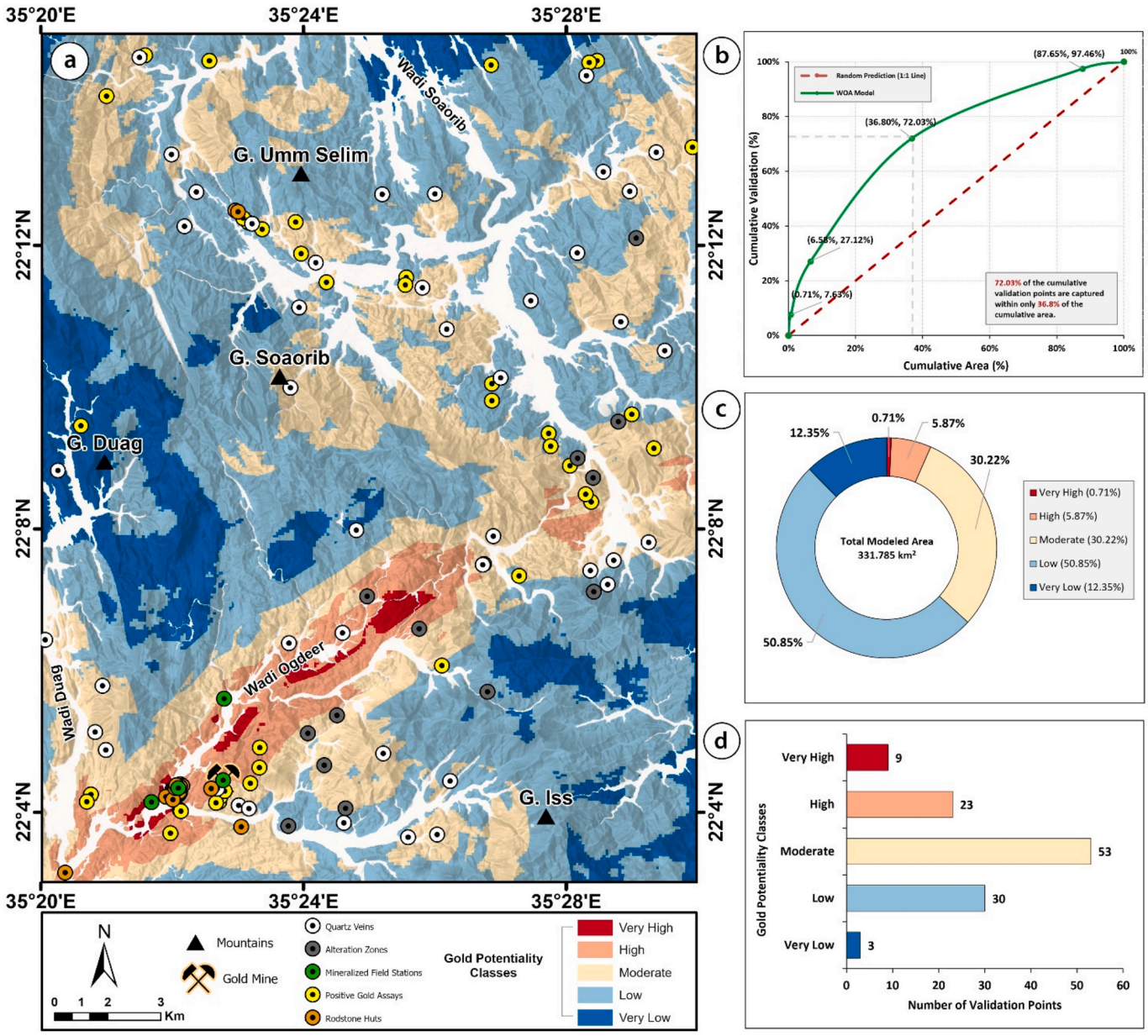


Fig. 19. Validation of the gold potentiality map (GPM). (a) Spatial distribution of the validation datasets, including the Soaorib Gold Mine, positive gold assay locations, quartz veins, alteration zones, mineralized field stations, and rodstone huts, overlaid on the GPM. (b) Success-rate curve showing the cumulative percentage of validation points relative to the cumulative modeled area. (c) Donut chart visualizing the percentage of the modeled area occupied by each class. (d) Bar chart showing the distribution of validation points across the five classes.

Table 5
Summary statistics for the validation of the GPM generated using the WOA model.

Class	Area (km^2)	Area (%)	Cumulative area (%)	No. of validation points	Validation (%)	Cumulative validation (%)
Very High	2.344	0.71%	0.71%	9	8%	8%
High	19.474	5.87%	6.58%	23	19%	27%
Moderate	100.262	30.22%	36.80%	53	45%	72%
Low	168.725	50.85%	87.65%	30	25%	97%
Very Low	40.981	12.35%	100%	3	3%	100%
Total	331.785	100%	100%	118	100%	100%

4) Integrating automated lineament extraction and detailed field-based structural analysis shows that the D1 deformation phase had the most significant impact on the regional structural framework, explaining the dominant tectonic trends observed across the area. Field observations suggest that gold mineralization is structurally controlled by localized high-strain transpressional structures developed during D3, including shear zones and reactivated thrust-related fabrics. Kinematic indicators and cross-cutting relationships confirm that the D3-related structures acted as effective conduits for

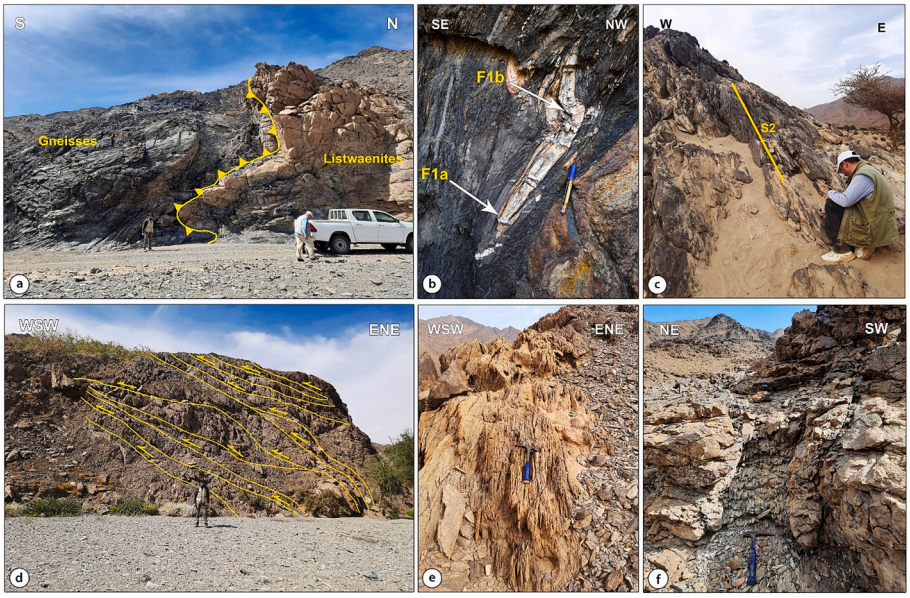


Fig. 20. Representative field photographs illustrate the polyphase deformation history of the study area, with the corresponding field station IDs and location-reference figure numbers given in parentheses. (a) T1 thrust contact juxtaposing listwaenites (right) against gneisses (left), reflecting early compressional nappe emplacement during arc accretion (ST-03; Fig. 5). (b) F1 fold interference pattern developed in graphite schist, resulting from superposition of early (F1a) and later (F1b) folding events, indicating polyphase ductile deformation during D1 (ST-03; Fig. 5). (c) Well-developed S2 penetrative foliation associated with D2 regional compression, affecting metavolcanic rocks (ST-22; Fig. 6). (d) T2 thrust sheets propagating toward the SE, recording intense crustal shortening during the main continental collision between East and West Gondwana (ST-04; Fig. 5). (e) S3 vertical shear foliation developed within listwaenites, indicating strong strain localization during transpressional deformation related to Hamisana Shear Zone activity (ST-01; Fig. 5). (f) Localized D3 shear zone showing well-developed shear fabric, reflecting intense shear-dominated deformation during the transpressional regime (ST-05; Fig. 5).

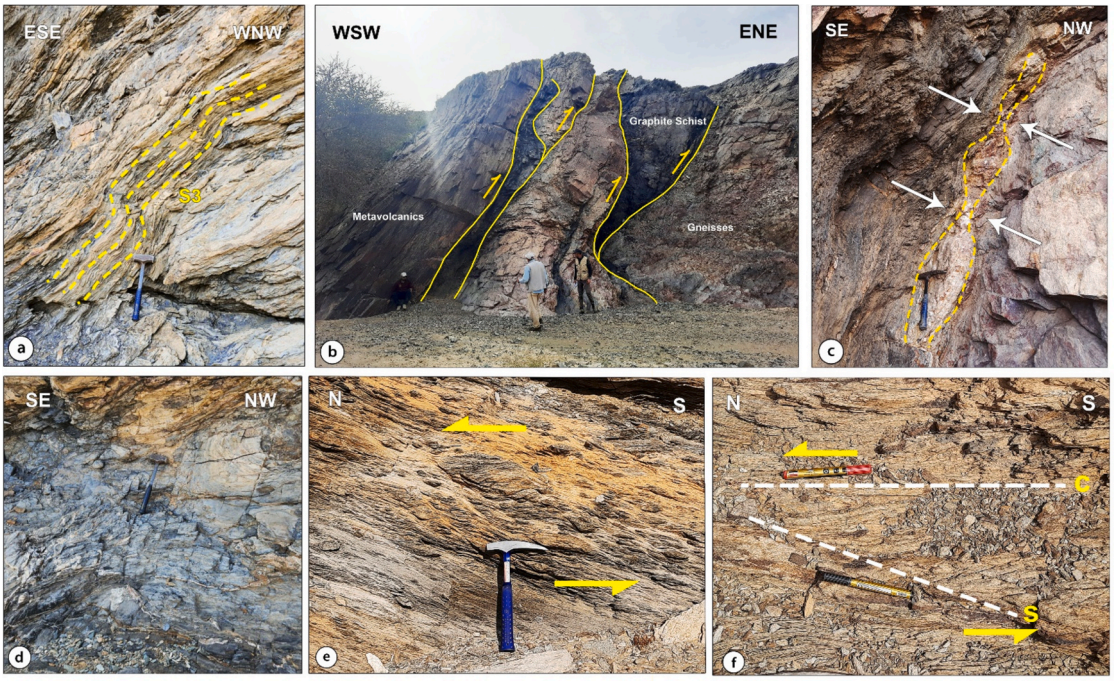


Fig. 21. Representative field photographs illustrate other D3-related structures and their role in structural control of gold mineralization, with the corresponding field station IDs and location-reference figure numbers given in parentheses. (a) S3 crenulation foliation developed in gneisses, reflecting refolding of earlier fabrics under transpressional deformation (ST-03; Fig. 5). (b) D3 positive flower structure affecting gneisses and graphite schist, formed by transpressional reactivation of earlier thrust systems during Najd-related deformation (ST-20; Fig. 6). (c) Boudinaged quartz vein developed within a transpressional shear zone, recording progressive deformation under combined compression and shearing (ST-20; Fig. 6). (d) Folded quartz veinlets hosted within highly sheared rocks, indicating *syn*-deformational quartz emplacement and continued strain during D3 (ST-03; Fig. 5). (e) D3 field-scale kinematic indicators within a shear zone, confirming dominant Najd-related transpressional wrench (ST-07; Figs. 5–6). (f) Well-developed D3 S–C fabric within a shear zone, recording intense strike-slip shearing (ST-06; Figs. 5–6).

mineralizing fluids, irrespective of the dominant regional structural orientations.

5) The GPM integrated the principal lithostructural factors controlling gold mineralization to delineate priority exploration targets. Independent validation using known gold occurrences revealed a strong spatial alignment between the High and Very High potentiality zones and the mineralization indicators, confirming the reliability of the proposed approach. The resulting model provides a practical regional-scale exploration framework that can support regional exploration in structurally complex terranes of the ANS.
6) Future exploration should prioritize detailed structural analysis, focused geochemical sampling, and subsurface drilling along the identified high-potential structural corridors to further assess and improve the gold prospectivity of the area.

Declaration of competing interest

The authors declare that they have no known competing financial interests or personal relationships that could have appeared to influence the work reported in this paper.

Acknowledgments

This study was financially supported through a scholarship from the AngloGold Ashanti Scholarship Program, Geology Department, Faculty of Science, Alexandria University. The authors express their heartfelt gratitude to the scholarship advisor, Prof. Hanafy M. Holail, for his continuous support. Gratitude is also given to Shalateen Mineral Resources Company (SMRC) for support and assistant during the progress of this work. Open access funding is supported by the University of Debrecen Program for Scientific Publication. We are grateful for the thoughtful comments and constructive suggestions from two anonymous reviewers, which significantly improved the manuscript. The Editor is sincerely appreciated for his valuable feedback and handling of the manuscript throughout the review stages.

Data availability

Data will be made available on request.

References

Abdeen, M.M., Abdelghaffar, A.A., 2011. Syn- and post-accretionary structures in the Neoproterozoic Central Allaqi–Heiani suture zone, southeast-ern Egypt. Precambr. Res. 185 (1–2), 118–138. https://doi.org/10.1016/j.precamres.2010.12.004.

Abdel-Karim, A.M., Ali, S., Helmy, H.M., El-Shafei, S.A., 2016. A fore-arc setting of the Gerf ophiolite, Eastern Desert, Egypt: evidence from mineral chemistry and geochemistry of ultramafites. Lithos 263, 483–497. https://doi.org/10.1016/j.lithos.2016.05.023.

Abdel-Karim, A.A.M., Azer, M.K., El-Shafei, S.A., 2021. Petrology and geochemistry of some ophiolitic metaperidotites from the Eastern Desert of Egypt: Insights into geodynamic evolution and metasomatic processes. Acta Geologica Sinica (english Edition) 95 (4), 1139–1157. https://doi.org/10.1111/1755-6724.14688.

Abdellatif, M., Elkhateeb, S.O., Hegab, M.A.E., Shebl, A., Mohamed, G., Mahdi, A.M., 2025. Revealing porphyry mineralization Cu–Au signatures via analyzing aeromagnetic and remote sensing data of Dara-Monqul, area Egypt. Sci. Rep. 15, 2755. https://doi.org/10.1038/s41598-025-90959-5.

Abd El Monsef, M., 2025. An Overview for Gold Mineralization in the Egyptian Segment of the Northern Continuation of the East African Orogen. In: Hamimi, Z., et al. Gold Deposits in Egypt. Sustainable Landscape Planning and Natural Resources Management. Springer, Cham. https://doi.org/10.1007/978-3-031-75972-7_6.

Abd El Monsef, M., Abdelnasser, A., 2021. Ore-forming mechanism and its relationship with deformational and metamorphic episodes at Haimur gold mine, Nubian Shield, Egypt. Geol. Magaz. 158 (3), 518–536.

Abd El Monsef, M., Slobodník, M., Salem, I.A., 2018. Hydrothermal evolution of granitoid-hosted gold mineralization in gidami area: an example for orogenic-gold deposits in Egypt. J. Afr. Earth Sc. 146, 132–149.

Abdel-Rahman, A.M., El-Desoky, H.M., Shebl, A., El-Awny, H., Amer, Y.Z., Csámer, Á., 2023. The geochemistry, origin, and hydrothermal alteration mapping associated with the gold-bearing quartz veins at Hamash district, South Eastern Desert, Egypt. Sci. Rep. 13 (1), 15221. https://doi.org/10.1038/s41598-023-42411-3.

Abdelsalam, M.G., Stern, R.J., 1996. Sutures and shear zones in the Arabian-Nubian Shield. J. Afr. Earth Sc. 23, 289–310. https://doi.org/10.1016/S0899-5362(97)00003-1.

Abd El-Wahed, M.A., Harraz, H., El-Behairy, M.H., 2016. Transpressional imbricate thrust zones controlling gold mineralization in the Central Eastern Desert of Egypt. Ore Geol. Rev. 78, 424–446. https://doi.org/10.1016/j.oregeorev.2016.03.022.

Abd El-Wahed, M.A., Zoheir, B., Pour, A.B., Kamh, S., 2021. Shear-related gold ores in the Wadi Hodein shear belt, South Eastern Desert of Egypt: analysis of remote sensing, field, and structural data. Minerals 11 (474). https://doi.org/10.3390/min11050474.

Abd El-Wahed, M., Kamh, S., Abu Anbar, M., Zoheir, B., Hamdy, M., Abdeldayem, A., Lebda, E.M., Attia, M., 2023. Multisensor satellite data and field studies for unravelling the structural evolution and gold metallogeny of the Gerf ophiolitic nappe, Eastern Desert, Egypt. Remote Sens. 15, 1974. https://doi.org/10.3390/rs15081974.

Abu-Alam, T., El Monsef, M.A., Grosch, E., 2018. Shear-zone hosted gold mineralization of the Arabian-Nubian Shield: Devolatilization processes across the greenschist–amphibolite-facies transition. In Geological Society, London, Special Publications (Vol. 478, pp. 287–313). Geological Society of London. https://doi.org/10.1144/SP478.13.

Ahmed, A.H., 2013. Highly depleted harzburgite–dunite–chromitite complexes from the Neoproterozoic ophiolite, South Eastern Desert, Egypt: a possible recycled upper mantle lithosphere. Precambr. Res. 233, 173–192. https://doi.org/10.1016/j.precamres.2013.05.001.

Alaoui, I.M., Akhssas, A., Bahi, A., Ibouh, H., Himyari, S.M., Khebbi, H., Sbabou, F.Z., 2025. Tectonic lineament mapping and identification of copper alteration minerals using PRISMA and Sentinel-2A satellite imagery in Alma inlier and Fouanou syncline (western Anti-Atlas, Morocco). Sci. Afr. 30, e02961. https://doi.org/10.1016/j.sciaf.2025.e02961.

Alarifi, S.S., Abdelkareem, M., Abdalla, F., Abdelsadek, I.S., Gahlan, H., Al-Saleh, A.M., Alotaibi, M., 2022. Fusion of multispectral remote-sensing data through GIS-based overlay method for revealing potential areas of hydrothermal mineral resources. Minerals 12, 1577. https://doi.org/10.3390/min12121577.

Alawy, M.K., Abdelwahed, M., Moghazi, A.-K.-M., Mohamed, F.H., Khamis, H., Shebl, A., 2025a. Utilizing remote sensing and field data for geological mapping and polyphase deformation analysis of Um Laseifa ophiolites, Eastern Desert, Egypt. Sci. Rep. 13, 18719. https://doi.org/10.1038/s41598-023-45838-0.

Alawy, M.K., Gomez-Barreiro, J., Hamimi, Z., Moghazi, A.K.M., Younis, M.H., Orench, I. P., Sánchez, S.B., 2025b. Tectonic reworking in the Arabian-Nubian Shield: an analysis of the textural record of the exhumation of the Meatiq Gneiss dome (Egypt). Gondw. Res. 143, 64–90. https://doi.org/10.1016/j.gr.2025.03.008.

Ali-Bik, M.W., Sadek, M.F., Ghabrial, D.S., 2014. Late Neoproterozoic metamorphic assemblages along the Pan-African Hamisana Shear Zone, south-eastern Egypt: metamorphism, geochemistry and petrogenesis. J. Afri-Can Earth Sci. 99, 24–38. https://doi.org/10.1016/j.jafrearsci.2013.08.010.

Ali, K.A., Azer, M.K., Gahlan, H.A., Wilde, S.A., Samuel, M.D., Stern, R.J., 2010. Age constraints on the formation and emplacement of Neoproterozoic ophiolites along the Allaqi-Heiani Suture, South Eastern Desert of Egypt. Gondw. Res. 18, 583–595. https://doi.org/10.1016/j.gr.2010.03.002.

Almond, D.C., Ahmed, F., Dawoud, A.S., 1984. Tectonic, metamorphic and magnetic styles in the Northern Red Sea Hills of Sudan. Bulletin of the Faculty of Science, King Abdulaziz University, Jeddah, 6, 449–458.

Asadzadeh, S., Zhou, X., Chabrillat, S., 2024. Assessment of the spaceborne EnMAP hyperspectral data for alteration mineral mapping: a case study of the Reko Diq porphyry Cu–Au deposit, Pakistan. Remote Sens. Environ. 314, 114389. https://doi.org/10.1016/j.rse.2024.114389.

Azer, M.K., Samuel, M.D., Ali, K.A., Gahlan, H.A., Stern, R.J., Ren, M., Moussa, H.E., 2013. Neoproterozoic ophiolitic peridotites along the Allaqi-Heiani suture, South Eastern Desert, Egypt. Miner. Petrol. https://doi.org/10.1007/s00710-012-0204-z.

Azer, M., Gahlan, H., Asimow, P., Al-Kahtany, K., 2017. The late Neoproterozoic Dahanib mafic–ultramafic intrusion, South Eastern Desert, Egypt: is it an Alaskan-type or a layered intrusion. Am. J. Sci. 317, 901–940. https://doi.org/10.2475/08.2017.02.

Badawi, M., Abdellatif, M., Shebl, A., Makroum, F., Shalaby, A., Németh, N., 2023. Mapping structurally controlled alterations sparked by hydrothermal activity in the Fatira–Abu Zawal area, Eastern Desert, Egypt. Acta Geol. Sin. – Engl. Ed. 97 (2), 662–678. https://doi.org/10.1111/1755-6724.15239.

Bannari, A., El-Battay, A., Saquaque, A., Miri, A., 2016. PALSAR-FBS L-HH mode and landsat-TM data fusion for geological mapping. Adv. Remote Sens. 5, 246–268.

Bonham-Carter, G.F., 1994. Geographic Information Systems for Geoscientists: Modelling with GIS. Computer Methods in the Geosciences, Vol. 13. Pergamon, Oxford.

Bosworth, W., Huchon, P., McClay, K., 2005. The Red Sea and Gulf of Aden basins. J. Afr. Earth Sc. 43 (1–3), 334–378. https://doi.org/10.1016/j.jafrearsci.2005.07.020.

Botros, N.S., 2002. Metallogeny of gold in relation to the evolution of the Nubian Shield in Egypt. Ore Geol. Rev. 19 (3), 137–164. https://doi.org/10.1016/S0169-1368(01)00035-X.

Botros, N.S., 2015. The role of the granite emplacement and structural setting on the genesis of gold mineralization in Egypt. Ore Geol. Rev. 70, 173–187. https://doi.org/10.1016/j.oregeorev.2015.04.014.

Carranza, E.J.M., 2008. Geochemical Anomaly and Mineral Prospectivity Mapping in GIS. Handbook of Exploration and Environmental Geochemistry, Vol. 11. Elsevier, Amsterdam.

Carranza, E.J.M., 2009. Controls on mineral deposit occurrence inferred from analysis of their spatial pattern and spatial association with geological features. Ore Geol. Rev. 35, 383–400. https://doi.org/10.1016/j.oregeorev.2009.01.001.

Carranza, E.J.M., Laborte, A.G., 2015. Data-driven predictive mapping of gold prospectivity, Baguio district, Philippines: application of random forests algorithm. Ore Geol. Rev. 71, 777–787. https://doi.org/10.1016/j.oregeorev.2014.08.010.

Chen, Q., Zhao, Z., Zhou, J., Zhu, R., Xia, J., Sun, T., Zhao, X., Chao, J., 2022. ASTER and GF-5 Satellite data for mapping hydrothermal alteration minerals in the Longtoushan Pb-Zn deposit, SW China. Remote Sens. 14 (5), 1253. https://doi.org/10.3390/rs14051253.

Chung, C.F., Fabbri, A.G., 2003. Validation of spatial prediction models for mineral prospectivity mapping. Nat. Resour. Res. 12, 13–19.

Clark, R.N., 1999. Spectroscopy of rocks and minerals, and principles of spectroscopy. In: Rencz, A.N. (Ed.), Manual of Remote Sensing, Vol. 3. John Wiley & Sons, pp. 3–58.

Collins, A.S., Pisarevsky, S.A., 2005. Amalgamating eastern Gondwana: the evolution of the Circum-Indian Orogens. Earth Sci. Rev. 71 (3–4), 229–270. https://doi.org/10.1016/j.earscirev.2005.02.004.

Dawoud, M., Khalaf, I.M., El-Dokouny, H.A., Shebl, A., El-Desouky, H., El-Lithi, M.A., 2023. Applications of remote sensing in lithological mapping of East Gabal Atud area, Central Eastern Desert, Egypt. Geo-Eco-Marina.

de Souza, S.R.C., Ducart, D.F., Botelho, N.F., 2024. Reflectance spectroscopy applied to mapping the hydrothermal alteration at the Mamão gold depos-it, Andorinhas Greenstone Belt, Carajás Mineral Province, Northern Brazil. Brazilian J. Geol. 54 (1), e20230048. https://doi.org/10.1590/2317-4889202420230048.

de Wall, H., Greiling, R.O., Sadek, M.F., 2001. Post-collisional shortening in the late Pan-African Hamisana high strain zone, SE Egypt: Field and magnetic fabric evidence. Precambr. Res. 107 (3–4), 179–194. https://doi.org/10.1016/S0301-9268(00)00141-8.

Diab, A., Moghazi, A.M., Ela, F., Alawy, M.K., Wu, F.-Y., Gahlan, H., Abd El-Wahed, M., Ali, K., 2026. Late neoproterozoic arc–fore-arc magmatism from the South Eastern Desert of Egypt: geochronology, whole-rock geochemistry, Hf–Nd isotopic compositions, and implications for Gondwana assembly. Gondw. Res. https://doi.org/10.1016/j.gr.2025.09.022.

El Aref, M., Abd El-Rahman, Y., Zoheir, B., Surour, A.A., Helmy, H.M., Abdelnasser, A., Ahmed, A.H., El-Ahmadi Ibrahim, M., 2020. Mineral resources in Egypt (I): metallic ores. In: Hamimi, Z., El-Barkooky, A., Martínez Frías, J., Fritz, H., Abd El-Rahman, Y. (Eds.), The Geology of Egypt. Regional Geology Reviews. Springer, Cham, pp. 521–587. https://doi.org/10.1007/978-3-030-15265-9_14.

El Baghdady, M.M., Omar, M.A., Awaga, G.A., Hanafi, A.M., El Bana, R.M., 2002. Geological and Geochemical Exploration at Madari and Soaorib areas, South Eastern Desert, Egypt. EGSMA, Internal Report No. 35/2002.

El-Desoky, H.M., Shebl, A., Abdel-Rahman, A.M., Fahmy, W., El-Awny, H., El-Sherif, A. M., El-Rahmany, M.M., Csámer, Á., 2022. Multiscale mineralogical investigations for mineral potentiality mapping of Ras El-Kharit–Wadi Khashir district, Southern Eastern Desert, Egypt. Egypt. J. Remote Sens. Space Sci. 25 (4), 941–960. https://doi.org/10.1016/j.ejrs.2022.09.002.

El-Desoky, H., Shebl, A., El-Awny, H., El-Rahmany, M., Soliman, O., 2023. Detecting oxides mineralization utilizing remote sensing and comprehensive mineralogical analysis: a case study around Mikbi-Zayatit district, South Eastern Desert, Egypt. Iraqi Geol. J. 56 (1E), 97–130. https://www.igj-iraq.org.

El Hebiry, M., 2021. Utilizing Advanced Remote Sensing Techniques for Detecting Geological and Structural Features Controlling Gold Mineralization, in Some Localities, South Eastern Desert, Egypt. Al Azhar University, Cairo, Egypt. Ph.D. Thesis.

El Kazzaz, Y.A.A., 2012. Shear zones related gold-bearing quartz veins in Shinai area, South Eastern Desert, Egypt. Egypt. J. Geol. 56, 67–89.

El Ramly, M.F., 1972. A new geological map for the basement rocks in the Eastern and Southwestern Deserts of Egypt. Ann. Geol. Surv. Egypt 2, 1–18.

El Shimi, K.A., Hassan, M.A., El Miligy, A.B., 2012. Report on Reconnaissance Survey of Ancient Gold Occurrences at Southeastern Corner of Eastern Desert, Egypt. Expedition No. G6/2010; Egypt Geological Survey: Cairo, Egypt, pp. 1–40.

Feng, J., Rogge, D., Rivard, B., 2018. Comparison of lithological map-ping results from airborne hyperspectral VNIR-SWIR, LWIR and combined data. Int. J. Appl. Earth Obs. Geoinf. 64, 340–353. https://doi.org/10.1016/J.JAG.2017.03.003.

Fossi, D.H., Djomo, H., Takodjou Wambo, J.D., Ganno, S., Kankeu, B., Nzenti, J.P., 2021. Structural lineament mapping in a sub-tropical region using Landsat-8/SRTM data: a case study of Deng-Deng area in Eastern Cameroon. Arab. J. Geosci. 14, 22. https://doi.org/10.1007/s12517-021-08848-9.

Fritz, H., Abdelsalam, M., Ali, K.A., Bingen, B., Collins, A.S., Fowler, A.R., Ghebreab, W., Hauzenberger, C.A., Johnson, P.R., Kusky, T.M., Macey, P., Muhongo, S., Stern, R.J., Viola, G., 2013. Orogen styles in the East African Orogen: a review of the Neoproterozoic to Cambrian tectonic evolution. J. Afr. Earth Sc. 86, 65–106. https://doi.org/10.1016/j.jafrearsci.2013.06.004.

Gahlan, H., Azer, M., Khalil, A.E.S., 2015. The Neoproterozoic Abu Dahr ophiolite, South Eastern Desert, Egypt: petrological characteristics and tectonomagmatic evolution. Mineral. Petrol. 109, 611–630.

Ge, W., Cheng, Q., Tang, Y., Jing, L., Gao, C., 2018. Lithological classification using Sentinel-2A data in the Shibanjing ophiolite complex in Inner Mongolia, China. Remote Sens. 10 (4), 638. https://doi.org/10.3390/rs10040638.

Ghebreab, W., Greiling, R.O., Solomon, S., 2009. Structural setting of Neoproterozoic mineralization, Asmara district, Eritrea. J. Afr. Earth Sci. 55 (2), 219–233. https://doi.org/10.1016/j.jafrearsci.2009.04.002.

Goldfarb, R.J., Groves, D.I., Gardoll, S., 2001. Orogenic gold and geologic time: a global synthesis. Ore Geol. Rev. 18 (1–2), 1–75. https://doi.org/10.1016/S0169-1368(01)00016-6.

Gray, D.R., Foster, D.A., Meert, J.G., Goscombe, B.D., Armstrong, R., Trouw, R.A.J. and Passchier, C.W.A., 2008. Damara orogen perspective on the assembly of southwestern Gondwana. In: Pankhurst R, Trouw R, et al, eds. West Gondwana Pre-Cenozoic Correlations Across the South Atlantic Region. Geol. Soc. London, Special Publ., 294, 257– 278.

Greiling, R.O., 1987. Shear zones in granitic rocks—a summary of field data. Geol. Rundsch. 76 (2), 593–608. https://doi.org/10.1007/BF01820586.

Groves, D.I., Goldfarb, R.J., Gebre-Mariam, M., Hagemann, S.G., Robert, F., 1998. Orogenic gold deposits: a proposed classification in the context of their crustal distribution and relationship to other gold deposit types. Ore Geol. Rev. 13 (1–5), 7–27. https://doi.org/10.1016/S0169-1368(97)00012-7.

Guanter, L., Richter, R., Moreno, J., 2006. Spectral calibration of hyperspectral imagery using atmospheric absorption features. Appl. Opt. 45 (10), 2360–2370. https://doi.org/10.1364/AO.45.002360.

Habashi, J., Jamshid Moghadam, H., Mohammady Oskouei, M., Pour, A.B., Hashim, M., 2024. PRISMA hyperspectral remote sensing data for mapping alteration minerals in Sar-e-Châh-e-Shur Region, Birjand, Iran. Remote Sens. 16 (7), 1277. https://doi.org/10.3390/rs16071277.

Harraz, H.Z., Ashmawy, M., 1994. Structural and lithogeochemical constraints on the localization of gold deposits at the El Sid–Fawakhir gold mine area, Eastern Desert, Egypt. Egypt. J. Geol. 38 (2), 629–648.

Harraz, H., El-Dahhar, M.A., 1993. Nature and composition of gold-forming fluids at Umm Rus area, Eastern Desert, Egypt: evidence from fluid inclusions in vein materials. J. Afr. Earth Sci. 16, 341–353. https://doi.org/10.1016/0899-5362(93)90054-T.

Harris, J.R., Grunsky, E., Behnia, P., Corrigan, D., 2015. Data- and knowledge-driven mineral prospectivity maps for Canada's North. Ore Geol. Rev. 71, 788–803. https://doi.org/10.1016/j.oregeorev.2015.01.004.

Harris, J.R., Strong, J., Thurston, P., Nymoen, K., Haugaard, R., Naghizadeh, M., Tuba, G., Behnia, P., Grunsky, E., Ayer, J., Smith, R., Sherlock, R., Reza-Mokhtari, A., 2025. Mineral prospectivity mapping and differential metal endowment between two greenstone belts in the Canadian Superior Craton. Nat. Resour. Res. 34, 97–120. https://doi.org/10.1007/s11053-024-10432-3.

Hassan, S.M., Ramadan, T.M., 2015. Mapping of the late Neoproterozoic basement rocks and detection of the gold-bearing alteration zones at Abu Marawat–Semna area, Eastern Desert, Egypt using remote sensing data. Arabi-an J. Geosci. 8 (7), 4641–4656. https://doi.org/10.1007/s12517-014-1519-4.

Helmy, H., El Mahallawi, M., 2003. Gabbro Akarem mafic–ultramafic complex, Eastern Desert, Egypt: a late Precambrian analogue of Alaskan-type complexes. Mineral. Petrol. 77, 85–108. https://doi.org/10.1007/s00710-001-0185-9.

Helmy, H.M., Kaindl, R., Fritz, H., Loizenbauer, J., 2004. The Sukari gold mine, Eastern Desert, Egypt: structural setting, mineralogy and fluid inclusion study. Miner. Deposita 39 (4), 495–511. https://doi.org/10.1007/s00126-004-0426-z.

Helmy, H.M., Abd El-Rahman, Y.M., Yoshikawa, M., Shibata, T., Arai, S., Tamura, A., Kagami, H., 2014. Petrology and Sm–Nd dating of the Genina Gharbia Alaskan-type complex (Egypt): insights into deep levels of Neoproterozoic island arcs. Lithos 198–199, 263–280. https://doi.org/10.1016/j.lithos.2014.04.007.

Hewson, R., Cudahy, T., Mizuhiko, S., Ueda, K., Mauger, A., 2006. Mapping geology associated with mangCanese mineralisation using spectral sensing techniques at Woodie Woodie, East Pilbara. Explor. Geophys. 37 (4), 389–400. https://doi.org/10.1071/EG06389.

Hilmy, M.E., Osman, A., 1989. Remobilization of gold from a chalcopyrite-pyrite mineralization Hamash gold mine, Southeastern Desert, Egypt. Mineral. Deposita 24, 244–249. https://doi.org/10.1007/BF00206386.

Hunt, G.R., 1977. Spectral signatures of particulate minerals in the visible and near infrared. Geophysics 42 (3), 501–513. 19.

Hunt, G.R., Salisbury, J.W., 1970. Visible and near-infrared spectra of minerals and rocks: I Silicate minerals. Mod. Geol. 1, 283–300.

Hunt, G.R., Salisbury, J.W., 1971. Visible and near-infrared spectra of minerals and rocks: II Carbonates. Mod. Geol. 2, 23–30.

Jan, N., Minallah, N., Gohar, N., Jan, N., Khan, S., Khan, S., Alibakhshikenari, M., 2024. Granite exposure mapping through Sentinel-2 visible and short wave infrared bands. Radio Sci. 59, e2023RS007864. https://doi.org/10.1029/2023RS007864.

Johnson, P.R., Woldehaimanot, B., 2003. Development of the Arabian–Nubian Shield: Perspectives on accretion and deformation in the northern East African Orogen and the assembly of Gondwana. In: M. Yoshida, B. F. Wind-ley, & S. Dasgupta (Eds.), Proterozoic East Gondwana: Supercontinent assembly and breakup (Vol. 206, pp. 289–325). Geological Society of London. https://doi.org/10.1144/GSL.SP.2003.206.01.15.

Johnson, P.R., Andresen, A., Collins, A.S., Fowler, A.R., Fritz, H., Ghebreab, W., Kusky, T., Stern, R.J., 2011. Late Cryogenian–Ediacaran history of the Arabian–Nubian Shield: a review of depositional, plutonic, structural, and tectonic events in the closing stages of the northern East African Orogen. J. Afr. Earth Sc. 61 (3), 167–232. https://doi.org/10.1016/j.jafrearsci.2011.07.003.

Johnson, P.R., Zoheir, B.A., Ghebreab, W., Stern, R.J., Barrie, C.T., Harries, R.D., 2017. Gold-bearing volcanogenic massive sulfides and orogenic-gold deposits in the Nubian Shield. S. Afr. J. Geol. 120 (1), 63–76. https://doi.org/10.25131/gssajg.120.1.63.

Karim, M., Rebai, N., Gannouni, S., Sedrette, S., Farah, I.R., 2021. Validation approach of the tectonic lineament extraction enhancement using Sentinel 2A images and modified 3 × 3 bidirectional prewitt filters. case study: Grombalia, Tunisia. J. Geogr. Inf. Syst. 13, 671–695. https://doi.org/10.4236/jgis.2021.136037.

Khedr, M.Z., Arai, S., 2013. Origin of Neoproterozoic ophiolitic peridotites in south Eastern Desert, Egypt, constrained from primary mantle mineral chemistry. Mineral. Petrol. 107, 807–828. https://doi.org/10.1007/s00710-012-0213-y.

Khedr, M.Z., Arai, S., 2016. Chemical variations of mineral inclusions in Neoproterozoic high-Cr chromitites from Egypt: evidence of fluids during chromitites genesis. Lithos 240–243, 309–326. https://doi.org/10.1016/j.lithos.2015.11.029.

Khedr, M.Z., Ghoneim, M.H., Hagag, W., Hauzenberger, C., Tamura, A., Ichiyama, Y., Takazawa, E., Kahal, A.Y., Abdelrahman, K., Zamzam, S., Morishita, T., El-Awady, A., 2024. Petrogenesis and tectonic evolution of mineralized mafic intrusions in the Eastern Desert of Egypt: implications for gold–sulfide genesis. Ore Geol. Rev. 173, 106273. https://doi.org/10.1016/j.oregeorev.2024.106273.

Khudeir, A., El Gaby, S., El Habaak, G., Gahlan, H., 2003. Metamorphic and tectonic history of Wadi Fiqo area, South Eastern Desert, Egypt. The Third International Conference on the Geology of Africa, Vol. 2, Assiut, Egypt, pp. 249–264.

Klemm, D., Klemm, R., 2013. In: Gold and Gold Mining in Ancient Egypt and Nubia: Geoarchaeology of the Ancient Gold Mining Sites in the Egyptian and Sudanese Eastern Deserts. Springer. https://doi.org/10.1007/978-3-642-22512-1.

Kröner, A., Todt, W., Hussein, I.M., Mansour, M., Rashwan, A.A., 1992. Dating of late Proterozoic ophiolites in Egypt and the Sudan using the single grain zircon evaporation technique. Precambr. Res. 59, 15–32. https://doi.org/10.1016/0301-9268(92)90076-7.

Kröner, A., Krüger, J., Rashwan, A.A.A., 1994. Age and tectonic setting of granitoid gneisses in the Eastern Desert of Egypt and south-west Sinai. Geologische Rundschau 83 (3), 502–513. https://doi.org/10.1007/BF01083223.

Kusky, T.M., Ramadan, T.M., 2002. Structural controls on Neoproterozoic mineralization in the South Eastern Desert, Egypt: an integrated field, Landsat TM, and SIR-C/X SAR approach. J. Afr. Earth Sc. 35 (1), 107–121. https://doi.org/10.1016/S0899-5362(02)00009-9.

Kusky, T.M., Abdelsalam, M., Stern, R.J., Tucker, R.D., 2003. Evolution of the East African and related orogens, and the assembly of Gondwana. Precambr. Res. 123, 81–85. https://doi.org/10.1016/S0301-9268(03)00062-7.

Li, Z.X., Bogdanova, S.V., Collins, A.S., Davidson, A., De Waele, B., Ernst, R.E., Fitzsimons, I.C.W., Fuck, R.A., Gladkochub, D.P., Jacobs, J., Karlstrom, K.E., Lu, S., Natapov, L.M., Pease, V., Pisarevsky, S.A., Thrane, K., Vernikovsky, V., 2008. Assembly, configuration, and break-up history of Rodinia: a synthesis. Precambr. Res. 160 (1–2), 179–210. https://doi.org/10.1016/j.precamres.2007.04.021.

Lillesand, T.M., Kiefer, R.W., Chipman, J.W., 2015. Remote Sensing and Image Interpretation, seventh ed. John Wiley & Sons, Hoboken, NJ.

Madani, A.A., Harbi, H.M., El-Dougdoug, A.M.A., Surour, A.A., Ahmed, A.H., 2021. Spectral characteristics of listvenites and serpentineites along ophiolite-decorated megashears (suture zones) in the Arabian Shield using ASD FieldSpec and satellite data. In: Hamimi, Z., Fowler, A.R., Liégeois, J.-P., Collins, A.S., Abdelsalam, M.G., Abd El-Wahed, M. (Eds.), The Geology of the Arabian-Nubian Shield. Regional Geology Reviews. Springer, Cham. https://doi.org/10.1007/978-3-030-72995-0_22.

Makhlouf, A., 2008. Petrology and tectonic evolution of the shield rocks of Gabal Soaorib area, South Eastern Desert, Egypt (Doctoral dissertation). Faculty of Science, Cairo University, Egypt.

Mamouch, Y., Attou, A., Miftah, A., Ouchchen, M., Dadi, B., Achkouch, L., Et-Tayea, Y., Allaoui, A., Boualoul, M., Randazzo, G., Lanza, S., Muzirafuti, A., 2022. Mapping of hydrothermal alteration zones in the Kelâat M'Gouna region using airborne gamma-ray spectrometry and remote sensing data: mining implications (Eastern Anti-Atlas, Morocco). Appl. Sci. 12 (3), 957. https://doi.org/10.3390/app12030957.

Mesbah, M., Ibrahim, E., Moghazi, A.M., Sandouly, H., Alawy, M.K., 2026. The late Neoproterozoic orogenic gold mineralization at the North Romite area, South Eastern Desert, Egypt: geological, geochemical, and structural constraints. J. Afr. Earth Sc. 236, 106023. https://doi.org/10.1016/j.jafrearsci.2026.106023.

Meyer, J.M., Kokaly, R.F., Holley, E., 2022. Hyperspectral remote sensing of white mica: a review of imaging and point-based spectrometer studies for mineral resources, with spectrometer design considerations. Remote Sens. Environ. 275, 113000. https://doi.org/10.1016/j.rse.2022.113000.

Miller, M.M., Dixon, T.H., 1992. Late Proterozoic evolution of the northern part of the Hamisana zone, northeast Sudan. constraints on Pan-African accretionary tectonics. J. Geol. Soc. Lond. 149, 743–750.

Ninomiya, Y., Fu, B., Cudahy, T.J., 2005. Detecting lithology with advanced spaceborne thermal emission and reflection radiometer (ASTER) multispectral thermal infrared "radiance-at-sensor" data. Remote Sens. Environ. 99 (1–2), 127–139. https://doi.org/10.1016/j.rse.2005.06.009.

Niroumand-Jadidi, M., Bovolo, F., Bresciani, M., Gege, P., Giardino, C., 2022. Water quality retrieval from landsat-9 (OLI-2) imagery and comparison to Sentinel-2. Remote Sens. 14. https://doi.org/10.3390/rs14184596.

Patchett, P.J., Chase, C.G., 2002. Role of transform continental margins in major crustal growth episodes. Geology 30 (1), 39–42.

Pour, A.B., Hashim, M., 2012. The application of ASTER remote sensing data to porphyry copper and epithermal gold deposits. Ore Geol. Rev. 44, 1–9. https://doi.org/10.1016/j.oregeorev.2011.09.009.

Pour, A.B., Park, Y., Park, T.-Y.-S., Hong, J.K., Hashim, M., Woo, J., Ayoobi, I., 2018. Regional geology mapping using satellite-based remote sensing approach in Northern Victoria Land, Antarctica. Polar Sci. 16, 23–46. https://doi.org/10.1016/j.polar.2018.02.004.

Pour, A.B., Zoheir, B., Pradhan, B., Hashim, M., 2021. Editorial for the special issue: multispectral and hyperspectral remote sensing data for mineral exploration and environmental monitoring of mined areas. Remote Sens. 13, 519. https://doi.org/10.3390/rs13030519.

Rowan, L.C., Mars, J.C., 2003. Lithologic mapping in the mountain pass, california area using advanced spaceborne thermal emission and reflection radiometer (ASTER) data. Remote Sens. Environ. 84 (3), 350–366. https://doi.org/10.1016/S0034-4257(02)00127-X.

Saaty, T.L., 1980. The Analytic Hierarchy Process: Planning, Priority Setting, Resource Allocation. McGraw-Hill, New York.

Sabet, A.H., Bordonosov, V.P., 1984. The gold ore formations in the Eastern Desert of Egypt. Ann. Geol. Survey Egypt 16, 35–42.

Shebl, A., Abdellatif, M., Elkhateeb, S.O., 2021. Multisource data analysis for gold potentiality mapping of Atalla area and its environs, Central Eastern Desert, Egypt. Minerals 11 (6), 641. https://doi.org/10.3390/min11060641.

Shebl, A., Abdelaziz, M.I., Ghazala, H., Araffa, S.A.S., Abdellatif, M., Csámer, Á., 2022. Multi-criteria groundwater potentiality mapping utilizing remote sensing and geophysical data: a case study within Sinai Peninsula, Egypt. Egypt. J. Remote Sens. Space Sci. 25 (4), 765–778. https://doi.org/10.1016/j.ejrs.2022.10.002.

Shebl, A., Abriha, D., Fahil, A.S., El-Dokouny, H.A., Elrasheed, A.A., Csámer, Á., 2023. PRISMA hyperspectral data for lithological mapping in the Egyptian Eastern Desert: evaluating the support vector machine, random forest, and XG boost machine learning algorithms. Ore Geol. Rev. 161, 105652. https://doi.org/10.1016/j.oregeorev.2023.105652.

Shebl, A., Abriha, D., Dawoud, M., Ali Hussein Ali, M., Csámer, Á., 2024. PRISMA vs. Landsat 9 in lithological mapping—A K-fold cross-validation im-plementation with Random Forest. Egypt. J. Remote Sens. Space Sci. 27 (3), 577–596. https://doi.org/10.1016/j.ejrs.2024.06.003.

Shebl, A., Abdellatif, M., Abriha, D., Dawoud, M., Ali, M.A.H., Mahmoud, A.S., Kristály, F., Csámer, Á., 2025. EnMap hyperspectral data in geological investigations: evaluation for lithological and hydrothermal alteration mapping in Neoproterozoic rocks. Gondw. Res. 143, 91–124. https://doi.org/10.1016/j.gr.2025.02.004.

Shalateen Mineral Resources Company (SMRC), 2018. Geological and Geo-chemical Report of Wadi Misah Concession (Internal Report).

Shalateen Mineral Resources Company (SMRC), 2021. Reconnaissance Survey on Meisah concession (Internal Report).

Shalateen Mineral Resources Company (SMRC), 2023. Field visit report of artisanal mining companies (Internal Report).

Stern, R.J., 1985. The Najd fault system, Saudi Arabia and Egypt: a late Precambrian rift-related transform system. Tectonics 4 (5), 497–511. https://doi.org/10.1029/TC004i005p00497.

Stern, R.J., 1994. Arc assembly and continental collision in the Neoproterozoic East African Orogen: implications for the consolidation of Gondwanaland. Annu. Rev. Earth Planet. Sci. 22, 319–351. https://doi.org/10.1146/annurev.ea.22.050194.001535.

Stern, R.J., Ali, K., 2020. Crustal evolution of the Egyptian Precambrian rocks. In: Regional Geology Reviews: the Geology of Egypt. Springer International Publishing, pp. 131–151. https://doi.org/10.1007/978-3-030-15265-9_4.

Stern, R.J., Hedge, G.E., 1985. Geochronologic constraints on late Precambrian crustal evolution in the Eastern Desert of Egypt. Am. J. Sci. 285 (2), 97–127. https://doi.org/10.2475/ajs.285.2.97.

Stern, R.J., Kroner, A., Manton, W.I., Reischmann, T., Mansour, M., Hussein, I.M., 1989. Geochronology of the late Precambrian Hamisana shear zone, Red Sea Hills, Sudan and Egypt. J. Geol. Soc. London 146 (6), 1017–1030. https://doi.org/10.1144/gsjgs.146.6.1017.

Stern, R.J., Nielsen, K.C., Best, E., Sultan, M., Arvidson, R.E., Kroner, A., 1990. Orientation of late precambrian sutures in the Arabian-Nubian shield. Geology 18, 1103–1106.

Sultan, M., Arvidson, R.E., Sturchio, N.C., 1986. Mapping of serpentinites in the Eastern Desert of Egypt by using Landsat thematic mapper data. Geology 14, 995.

Sun, T., Chen, F., Zhong, L., Liu, W., Wang, Y., 2019. GIS-based mineral prospectivity mapping using machine learning methods: a case study from Tongling ore district, eastern China. Ore Geol. Rev. 109, 26–49. https://doi.org/10.1016/j.oregeorev.2019.04.003.

Surour, A.A., Madani, A.A., El Sobky, M.A., 2025. Integration of mineralogical, geochemical and ASD reflectance spectra data for characterization and evolution of Neoproterozoic serpentinites and listwaenites at Wadi Kalalat area, South Eastern Desert of Egypt. Geochemistry 85, 126262. https://doi.org/10.1016/j.chemer.2025.126262.

Tadesse, S., Milesi, J.P., Deschamps, Y., 2003. Geology and mineral potential of Ethiopia: a note on geology and mineral map of Ethiopia. J. Afri-Can Earth Sci. 36 (4), 273–313. https://doi.org/10.1016/S0899-5362(03)00083-1.

Traore, M., Takodjou Wambo, J.D., Ndepete, C.P., Tekin, S., Pour, A.B., Muslim, A.M., 2020. Lithological and alteration mineral mapping for alluvial gold exploration in the south east of Birao area, Central African Republic using Landsat-8 Operational Land Imager (OLI) data. J. Afr. Earth Sc. 170, 103933. https://doi.org/10.1016/j.jafrearsci.2020.103933.

United States Geological Survey (USGS), 2022. Landsat 9 data users handbook (Version 1.0, LSDS-2082). USGS Department of the Interior. https://www.usgs.gov/media/files/landsat-9-data-users-handbook.

van der Meer, F.D., van der Werff, H.M.A., van Ruitenbeek, F.J.A., Hecker, C.A., Bakker, W.H., Noomen, M.F., van der Meijde, M., Carranza, E.J.M., de Smeth, J.B., Woldai, T., 2012. Multi- and hyperspectral geologic remote sensing: a review. Int. J. Appl. Earth Obs. Geoinf. 14, 112–128. https://doi.org/10.1016/j.jag.2011.08.002.

Xu, H., Ren, M., Lin, M., 2024. Cross-comparison of Landsat-8 and Landsat-9 data: a three-level approach based on underfly images. Gisci. Remote Sens. 61 (1), 1–20. https://doi.org/10.1080/15481603.2024.2318071.

Yajima, T., Yamaguchi, Y., 2013. Geological mapping of the Francistown area in north-eastern Botswana by surface temperature and spectral emissivity information derived from ASTER thermal infrared data. Ore Geol. Rev. 53, 134–144. https://doi.org/10.1016/j.oregeorev.2013.01.001.

Zimmer, M., Kröner, A., Jochum, K.P., Reischmann, T., 1995. The Gabal Gerf complex: A Precambrian N-MORB ophiolite in the Nubian Shield, NE Africa: v. 123, p. 29–51.

Zoheir, B.A., 2008. Structural controls, hydrothermal alteration, and fluid evolution of gold mineralization in the Um El Tuyor mine area, Eastern Desert of Egypt. Ore Geol. Rev. 34 (3–4), 410–429. https://doi.org/10.1016/j.oregeorev.2008.01.002.

Zoheir, B., 2011. Transpressional zones in ophiolitic mélange terranes: potential exploration targets for gold in the South Eastern Desert, Egypt. J. Geochem. Explor. 111, 23–38. https://doi.org/10.1016/j.gexplo.2011.07.003.

Zoheir, B.A., 2012a. Controls on lode gold mineralization, Romite deposit, South Eastern Desert, Egypt. Geosci. Front. 3 (5), 571–585. https://doi.org/10.1016/j.gsf.2012.03.003.

Zoheir, B.A., 2012b. Lode-gold mineralization in convergent wrench structures: examples from South Eastern Desert, Egypt. J. Geochem. Explor. 114, 82–97. https://doi.org/10.1016/j.gexplo.2011.10.006.

Zoheir, B., Emam, A., 2014. Field and ASTER imagery data for the setting of gold mineralization in Western Allaqi–Heiani belt, Egypt: A case study from the Haimur deposit. Journal of African Earth Sciences 99, 150–164. https://doi.org/10.1016/j.jafrearsci.2013.06.006.

Zoheir, B.A., Klemm, D.D., 2007. The tectono-metamorphic evolution of the central part of the Neoproterozoic Allaqi-Heiani suture, South Eastern Desert of Egypt. Gondw. Res. 12, 289–304. https://doi.org/10.1016/j.gr.2006.10.002.

Zoheir, B., Emam, A., El-Amawy, M., Abu-Alam, T., 2018. Auriferous shear zones in the central Allaqi–Heiani belt: orogenic gold in post-accretionary structures, SE Egypt. J. Afr. Earth Sc. 146, 118–131. https://doi.org/10.1016/j.jafrearsci.2017.10.017.

Zoheir, B.A., Johnson, P.R., Goldfarb, R.J., Klemm, D.D., 2019. Orogenic gold in the Egyptian Eastern Desert: widespread gold mineralization in the late stages of Neoproterozoic orogeny. Gondw. Res. 75, 184–217. https://doi.org/10.1016/j.gr.2019.06.002.

Zoheir, B., Abd El-Rahman, Y., Kusky, T., Xiong, F., 2022. New SIMS zircon U-Pb ages and oxygen isotope data for ophiolite nappes in the Eastern Desert of Egypt: implications for Gondwana assembly. Gondw. Res. 105, 450–467. https://doi.org/10.1016/j.gr.2021.09.022.